Highly Efficient All-Polymer Solar Cells based on Wide Bandgap Donor Copolymers Containing Selenophene Moieties

Shripathi Ramakrishnan

A thesis

submitted in partial fulfillment of the

requirements for the degree of

Master of Science in Chemical Engineering

University of Washington

2020

Committee:

Samson A. Jenekhe

Vincent C. Holmberg

Program Authorized to Offer Degree:

Chemical Engineering

University of Washington

Abstract

Highly Efficient All-Polymer Solar Cells based on Wide Bandgap Donor Copolymers Containing Selenophene Moieties

Shripathi Ramakrishnan

Chair of the Supervisory Committee:
Samson A. Jenekhe
Department of Chemical Engineering

All-polymer solar cells (all-PSCs) based on binary blends of napthalenediimide biselenophene acceptor copolymer (PNDIBS) with wide-bandgap selenophene-containing donor copolymers, PBDB-S and PBDBS-T, were fabricated and characterized to investigate the effects of alkylselenyl side-chain and selenophene π-spacer on the respective polymer donors and compared to their thiophene equivalent, PBDB-T. Compared to PBDB-S, PBDBS-T displayed a narrower bandgap and red-shifted absorption owing to an upshifted HOMO by 0.13 eV. Both donors displayed significantly enhanced hole mobilities compared to PBDB-T, resulting in significantly higher photocurrent values of 17.51 mA/cm^2 and 18.31 mA/cm^2. Additionally, the superior crystallinity, and phase-separated morphology conferred by PBDBS-T resulted in

efficient exciton dissociation and charge transport, enabling greater fill factors up to 63.5% and 9.5% efficiency. These results indicate that a selenophene π-spacer in a D-A polymeric backbone is beneficial to the photovoltaic properties, photophysics, and morphology of all-PSCs and is a promising molecular design strategy to develop highly efficient all-PSCs.

TABLE OF CONTENTS

LIST OF FIGURES

LIST OF TABLES

ACKNOWLEDGEMENTS

I would like to take this opportunity to express my heartfelt gratitude to my MS thesis advisor, Dr. Samson A. Jenekhe, for his capable guidance and support. His encouragement and insightful suggestions have allowed to me explore new avenues of research and helped me grow at a personal level.

I also extend my sincere gratitude to Dr. Vincent C. Holmberg for taking time off his busy schedule to serve on my thesis committee and provide valuable suggestions.

I would like to acknowledge some past and present members of the Jenekhe lab, Hyunjong Lee, Dr. Nagesh B. Kolhe, Omkar Bhambure, Sarah M. West, Xiaomei Ding, Mary Nguyen and Duyen K. Tran, who have enriched my journey through research with their insightful discussions and incisive analyses. Working in tandem with such a motivated and intellectual team has truly broadened my view of the field.

I would like to thank the National Science Foundation and the Office of Naval Research for their grant support that made this research possible.

Lastly, I wish to show my gratitude to my friends and family for their unconditional moral support that has made my time abroad and at the University of Washington truly wonderful.

Chapter 1. Introduction.

1.1. Background.

Harvesting energy from sunlight using photovoltaics (PV) have garnered great interest to scavenge energy from renewable and low-cost sources, triggered by the gradual depletion of fossil fuels and ever-increasing carbon footprint. Photovoltaic technology may be broadly classified into three generations, and among them, organic photovoltaics (OPVs) are classified as the emerging third-generation photovoltaic technology. Some of the intrinsic properties of organic semiconductors have evoked serious consideration as viable alternatives or complements to the established inorganic photovoltaics (IPVs).[1] The mechanical advantages offered by OPVs (lightweight, high flexibility, transparency)[2–5] and the relative ease of fabricating these devices through low-cost solution processing have distinguished organic photovoltaics as an ergonomically feasible alternative for mass production and roll-to-roll manufacture.[6,7] Thus, OPVs can be used to realize portable, wearable energy sources or window tinting applications, which were previously difficult using IPV technology.

Subsequently, extensive efforts were dedicated to the development of bulk heterojunction polymer solar cells (PSCs), which comprised of an interpenetrating network of n-type electron-accepting semiconductors and p-type electron-donating semiconductors, formed through the admixture of the phases in solution to form a blend. Early studies extensively used a combination of semiconducting donor polymers and buckminsterfullerene derivatives. Phenyl-C_{61}-butyric acid methyl ester (PCBM) was used ubiquitously in PSCs as an acceptor material because of to its deep lowest unoccupied molecular orbital (LUMO) and high electron mobility.[8–11] This motivated the investigation of molecular design strategies in the synthesis of donor polymers to facilitate efficient

charge separation and exciton dissociation. However, the significant drawbacks of PCBM systems, namely difficulty in synthesis, limited absorption window in the visible range, low chemical and electronic tunability, and poor solubility in conventional halogenated solvents reinforced the need to pioneer novel n-type semiconductors.[12–15] Among them, the development of systems composed of a p-type polymeric electron donor and an n-type electron acceptor polymer dubbed as All-Polymer Solar Cells (all-PSCs) has risen to prominence. All-PSCs displayed superior thermal, mechanical, photostability, and very high chemical tunability compared to their fullerene counterparts. However, their performances still lag behind those of Fullerene-acceptor and small-molecule acceptor (SMA) solar cells and this reinforces the need to investigate novel molecular design strategies and optimization techniques to achieve better power conversion efficiencies.[16,17]

1.2. Organic Solar Cell fundamentals: Architecture and working principle:

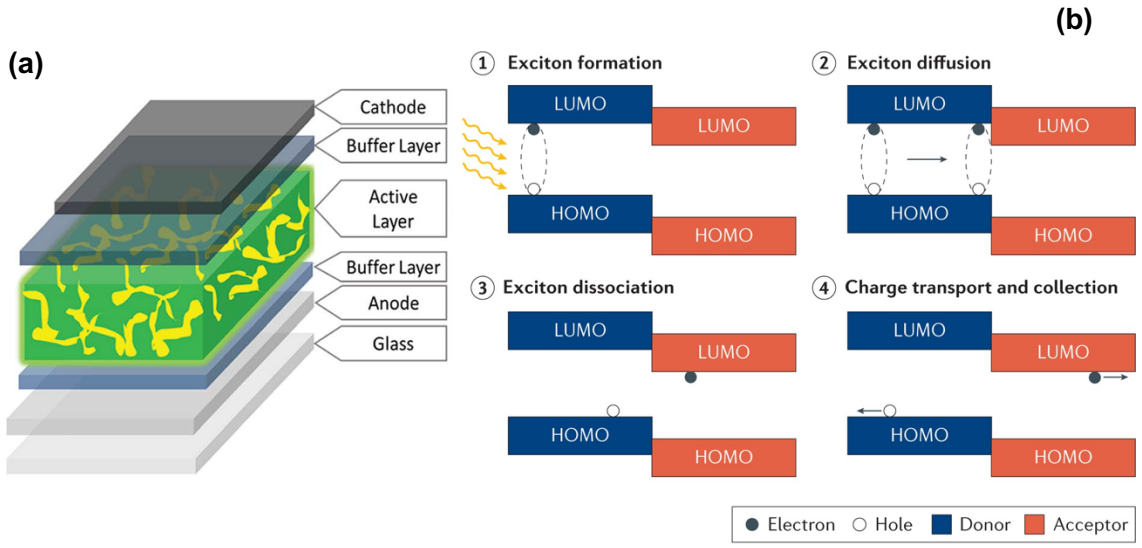

Figure 1. (a) Structure and (b) working mechanism of a bulk-heterojunction organic solar cell.

Figure 1a. illustrates the schematic representation of an organic solar cell, which consists of a bulk heterojunction (BHJ) active layer composed of an electron-rich and an electron-deficient

species, flanked by charge selective interfacial layers and electrodes to collect the photogenerated charges. In an ideal BHJ structure, upon blending and casting of the active layer, the phases undergo nanoscale phase separation to form a bicontinuous two-phase interpenetrating network with a reasonably large interfacial area between the donor and acceptor domains to facilitate efficient charge dissociation provided by hole and electron pathways. The holes and electrons then migrate through the donor rich and electron-rich phases upon illumination towards their respective electrodes where they are harvested.[12]

Thus, the working mechanism of an organic solar cell may be summarised into the following steps as represented by Figure 1b: (1) The photoexcitation induced by illumination generates a Coulombically bound electron-hole pair (dubbed exciton) by the donor phase. (2) The exciton diffuses to the donor-acceptor interface, (3) whereupon it dissociates to form a geminate pair. (4) The free charges are then collected at their respective electrodes. It should be noted though that the feasibility of (3) is dependent on the binding energy E_b of the exciton. While it is insignificant for inorganic and perovskite solar cells, organic materials exhibit relatively large binding energies. For instance, E_b of poly(3-hexylthiophene) P3HT is in the range of 0.7eV[18], which can prove to be detrimental to charge separation in a single component system. Therefore, it is critical to select and blend active layer materials that are so chosen such that there is a sufficient driving force to facilitate charge dissociation. The driving force for the process may be quantitatively determined by studying the HOMO (Highest Occupied Molecular Orbital) and LUMO (Lowest Unoccupied Molecular Orbital) offset between the acceptor and donor respectively.

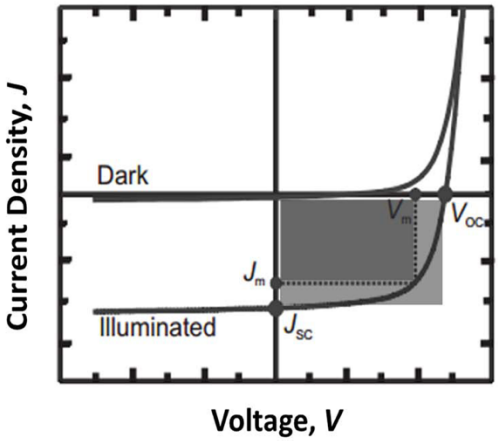

Figure 2. Parameters of interest to evaluate OPV performance.

The performance of an organic solar cell may be quantified by investigating the power conversion efficiency (PCE%) of the device which is represented as follows:

$$PCE = \frac{J_{sc} * V_{oc} * FF}{P_{in}}$$

P_{in} refers to the power density of the incoming solar illumination, J_{sc} the short-circuit current, V_{oc} the open circuit potential, and FF is the fill factor. (The latter is denoted as $P_{max}/(J_{sc}*V_{oc})$ with P_{max} as the maximum power density) The J_{sc} is limited by the ability and the rate at which the incoming photons are absorbed by the donor and acceptor materials, the efficiency of exciton dissociation, and the effectiveness of the flanking charge transport layer and electrodes in charge collection.[19] The V_{oc} on the other hand is dependent on the donor-acceptor energy offset, interfacial area, and the radiative and non-radiative recombination processes.[20] Thus, a compromise must be reached between J_{sc} and V_{oc}. The most efficient OPVs feature materials that absorb as much radiation as possible in the visible and near-infrared regions of the solar spectrum (possibly with a wide bandgap material) and deeper energy levels.[21]

Therefore, it is of interest to understand the interactions between donor and acceptor phases from both a device engineering perspective and at a molecular level to maximize light harvesting and achieve an optimal morphology between the phases to minimize undesirable recombination processes that inhibit photovoltaic effects.

1.3. Major hurdles:

Polymer solar cells (PSCs) have garnered much attention in recent decades as novel alternative energy technology for the development of polymer semiconductors and organic electronic devices given their unique advantages of lightweight, flexibility ease of processing from solution, and cost-effectiveness. Among PSCs, all-polymer solar cells (all-PSCs) where the active layers are comprised of a p-type donor copolymer and n-type acceptor copolymer have been a cynosure of increasing scrutiny owing to their advantages over their fullerene counterparts[22–25] namely thermal and mechanical robustness[3,26], chemical and electronic tunability, morphological stability in air [27–30] and feasible rheological properties[26]. Furthermore, in comparison to fullerene acceptor-based and non-fullerene small-molecule acceptor (NFA-SMA) based solar cells, all-PSCs present some unique morphological, thermal, and stretchable stabilities, making them serious contenders for flexible and wearable optoelectronic device applications.

Over the last several years, significant strides have been made towards the development of high-performance all-PSCs through the development of new combinations of donor and acceptor materials, manipulating molecular design to tune energy levels, morphology, and crystallinity, and novel device and thin-film optimization pathways.[29,31–34] This facilitated significantly heightened power conversion efficiency (PCE) values and improved device stability to as high as 14% PCE with up to 80% PCE retention at elevated temperatures.[35] Some of the successful n-type polymer

acceptors utilized in high-performance all-PSCs were usually based on naphthalene diimide (NDI) arylene copolymer acceptors. The most prominent member among this family of acceptor copolymers included poly{[N, N0-bis (2-octyldodecyl)-naphthalene-1,4,5,8-bis(dicarboximide)-2,6-diyl]-alt-5,50-(2,20-bithiophene), commercially known as N2200 which exhibited high electron mobility, wide visible-near infra-red range absorption and good solubility comparable to those of fullerene-based and non-fullerene small molecule acceptors.[34,36] Indeed, PCEs as high as 11.76% has been reported by pairing N2200 with pyrrolo[3,4-f]benzotriazole-5,7-dione (TzBI)-based polymer donor.[34] However, N2200 exhibited some significant drawbacks such as low absorption coefficient and strong crystallization tendency that makes regulation of OPV morphology quite difficult. [31,32]

Our group has demonstrated the efficacy of various all-PSC systems with PCEs as high as 9-10% using NDI-biselenophene (PNDIBS) based copolymer acceptor[37,38] and random copolymer variants of the same (BSSx) [29] with the commercially available PBDB-T. The acceptor PNDIBS displayed high field-effect mobility (0.07 cm^2/Vs), stronger absorption coefficient (c.a. 1.1 x 10^5 cm^{-1}) and greater face-on tendency compared to N2200, as evidenced by GIWAXS[38,39]. As the number of studies on this family of polymers is still growing, it is of interest to further expand on the scope of PNDIBS acceptor beyond that of PBDB-T donor. It is possible to further enhance the PCE through the exploration of rational molecular design strategies to construct novel p-type donor copolymers that are compatible with typical n-type acceptors. As PNDIBS has dual peaks with a π-π^* transition peak between 300-450 nm and an intramolecular charge transfer peak between 700-850 nm, it is highly desirable to develop medium band gap donor polymers that have complementary absorption with high and balanced hole/electron mobilities to maximize photovoltaic performance.

Furthermore, an equally important consideration lies in the ability of the donor and acceptor polymers to form a phase separated and interpenetrating donor-acceptor network to construct pathways that facilitate effective exciton dissociation and reduction of recombination. This is another aspect of designing state-of-the-art all-PSCs, where solution processing, choice of solvents, incorporation of suitable additives and selection of pre-treatment pathways become important considerations to regulate and tune the film morphology to maximize charge collection. Enabling differential aggregation rates of either component in the polymeric blend by mixed solvent processing or using volatile additives may have some dramatic effects on film morphology. Such techniques allow a greater degree of control over the morphology and crystallization kinetics of the bulk phases to achieve optimal pathways. Thus, molecular design in accompaniment with device engineering and active-layer processing is key to elevating photovoltaic performance in all-PSCs.

1.4. Research objectives:

Chapter 2 deals with the optimization of device processing, performance studies, and morphology of all-polymer solar cells based on Polynapthalene diimide-biselenophene (PNDIBS) acceptor. The specific scope of this work includes **investigating the impact of selenophene-containing donor polymers on the performance of all-polymer solar cells Based on naphthalene diimide-biselenophene copolymer acceptor**.

Two p-type polymer donors based on PBDB-T were modified through selenophene substitution on the conjugated side chain (PBDB-S) and the backbone or spacers (PBDBS-T) of the BDT building block respectively.

This study discusses the systematic device optimization and processing, photovoltaic properties, and charge photophysics of all-PSCs with PBDB-T, PBDB-S, and PBDBS-T copolymer donors paired with PNDIBS acceptor copolymer. Additionally, aspects of surface morphologies such as surface roughness, crystallite ordering, and domain sizes have also been characterized to reveal insights on the nature of interactions between different donors and PNDIBS acceptor. The results reveal the subtle differences in film ordering and aggregation kinetics originating from selenophene inclusion at different sites of the BDT building block, as evidenced by the differences in pre-treatment for the representative all-PSCs (thermal annealing for PBDB-S and film aging for PBDBS-T). Furthermore, as elucidated by the SCLC results and XRD data, the enhancement in bulk crystallinity of PBDBS-T:PNDIBS systems has in resulted in to significant improvements in PCE. The balanced charge transport, superior photophysics and morphology have enabled inverted all-PSCs with a PCE of 9.14%, which is a 13% increase over its unsubstituted counterpart.

Chapter 2. Impact of selenophene containing wide bandgap donor copolymer on the performance, photophysics and morphology of All-Polymer Solar Cells.

2.1. Introduction.

All-Polymer Solar Cells (All-PSCs), where the active layer consists of a binary blend of a p-type conjugated donor polymer and n-type conjugated acceptor polymer, have attracted a great deal of attention recently as a technologically viable alternative to fullerene-based/small-molecule non-fullerene acceptor (SM-NFA) based organic solar cells.[22–25,40] This is ascribed to their superior thermal and mechanical robustness,[2,3,5] enhanced light-harvesting and absorption, feasible rheological properties[26,27] and versatility with respect to tuning of the molecular, electronic and morphological properties.[27–30] Although major strides towards the development of high performance All-Polymer Solar Cells have been made recently leading to PCEs of 10-14%,[29,31–36,41] their performance still lags behind those of NFA-SMA devices quite significantly. Nevertheless, they remain great prospects for large-scale optimization and manufacture.[5,26]

Some of the key bottleneck parameters limiting All-PSC performance include the photocurrent and fill factor (FF),[23,24,42] while significant ground has been made towards addressing their optical band-gap (E_g^{opt}) energy loss ($E_{loss} = E_g^{opt} - eV_{oc}$), resulting in improved open-circuit voltages (V_{oc}).[29,32,37,38] A major challenge involves the simultaneous of increase the short-circuit current (J_{sc}) and fill factor (FF), both of which are critically dependent on the blend morphology.[16,17,43,44] Indeed, the photocurrents generated remain relatively low even among some of the best all-PSCs reported to date.[31,33,34]

In the past, our group had reported and synthesised an NDI-arylene acceptor copolymer, poly-naphtalenediimide biselenophene, PNDIBS, which is the selenophene analogue of the commercial P(NDI-2OD-T2). PNDIBS was found to possess a narrow bandgap of 1.40 eV, more intense absorption coefficient (α) of c.a. 1 x 10^5 cm^{-1} and a red-shifted ICT band in comparison to P(NDI-2OD-T2) with a high n-channel field effect mobility of 0.07 mA/cm^2s. Consequently, a maximum PCE up to 9.4% was obtained when paired with a suitable wide-bandgap donor polymer, PBDB-T with complementary absorption.[37] Specifically, as highlighted by the results in the subsequent section, optimized all-polymer solar cells based on the reference PBDB-T:PNDIBS blend yielded a fairly high $PCE_{average}$ of 8.08%, when synthesised and fabricated under slightly different conditions, in accord with another study performed by our group.[38] However, the optimized devices showed modest values for short-circuit current density (J_{sc}) and fill factor (FF).

It is possible to facilitate an improvement in performance by employing a similar suitable wide-bandgap donor copolymer with a rational molecular design approach. Thus, to facilitate ease of comparison and understanding of the evolution of the photovoltaic and morphological properties, this work has a focus on a family of polymers with minimal structural and molecular difference in comparison to the PBDB-T donor copolymer. PBDB-T is a D-A copolymer composed of benzo[1,2-*b*:4,5-*b*′]dithiophene (BDT) donor block flanked by a pair of thiophene units on the conjugated side chain and a benzo[1,2-*c*:4,5-*c*′]dithiophene-4,8-dione (BDD) acceptor block, connected by two thiophenes π-spacers. As the BDT building block has led to the development of several high performing fullerene solar cells, BDT based donors have also been used extensively to construct state-of-the-art all-PSCs.[45–48] The main reasons attributed to the success of the BDT skeleton in achieving high-performing wide-bandgap donors in OPVs devices

lie in their moderate crystallinity, good planarity, strong π-π stacking, charge transport and good thermodynamic compatibility with NDI based acceptors. [16,49]

A promising strategy to improve the J_{sc} and FF of All-PSCs involves the incorporation of selenophene in place of thiophene into the molecular structure of the donor polymer.[50–54] Selenophene substitution has been used enhance the photovoltaic properties, particularly with SM-NFA [55–58] and has been proven to be a powerful molecular design strategy. Recent studies have revealed the red-shifted absorption band and low bandgap of conjugated polymers substituted with selenophene in place of thiophene owing to its enhanced ground state quinoid resonance characteristics. Thus, the resulting polymeric chains exhibit longer conjugation and planarity. As a result of these effects, conjugated donor polymers exhibit well-ordered aggregation and improved charge transport properties that elicit a superior J_{sc}.[51,59] Furthermore, Se substitution results in enhanced crystallinity of the blend components and formation of a favorable phase separated blend morphology through Se-Se intermolecular interactions with high domain purity.[60] The stronger heteroaromatic interactions of atomic selenium also translate to improved charge transport and interchain interactions. Thus, utilizing the strong aggregating property and inherent crystallinity conferred by selenophenes in conjunction with an amorphous electron donating core such as benzodithiophene (BDT) can lead to the synthesis of high mobility donor materials with strong absorption.[24,53,54]

Thus, selenophene has been used as an effective building in the molecular design of several high performance donors that have achieved stellar PCEs in both fullerene-based and non-fullerene based PSCs. For instance, Li et al. have reported the effects of a selenophene-containing donor copolymer, PBPD-Se with a selenophene π-spacer as compared to its thiophene analogue on the PCE of fullerene-based PSCs. PBPD-Se was found to exhibit a narrower bandgap of 1.77 eV and

enhanced hole mobility (1.12×10^{-3} $cm^2/(V\ s)$) over its thiophene counterpart, PBPD-Th, leading to an improved J_{sc} from 12.4 mA/cm^2 to 14.9 mA/cm^2, FF from 0.71 to 0.73 and thus a better PCE of 9.8% over 8.4%.[54] Also, Peng et al. modified the known J51 donor copolymer (PBDT-FTAZ) by incorporating alkylselenyl conjugated side-chains onto the BDT building block to obtain PBDT-Se-TAZ and PBDTS-Se-TAZ and reported non-fullerene PSCs based on ITIC-Th with high J_{sc}s of 18.63 and 19.51 and FFs of 0.67 and 0.75.[61] While significant research has been carried out on selenophene-containing donors in both fullerene and non-fullerene based PSCs enabling PCEs as high as 12%,[50,51,58,61] such molecular design strategies have yet to be explored in all-polymer solar cells. Surprisingly, there are limited investigations on their effects on the photovoltaic performance and morphology in conjunction with the widely used naphthalenediimide (NDI) copolymer acceptors notwithstanding the thermodynamically favoured interaction and suppressed largescale phase-segregation between BDT and NDI based polymers. [62]

Herein, two novel wide bandgap p-type donor copolymers, PBDB-S and PBDBS-T, were synthesized based on PBDB-T with selenophene on the conjugated side chain and π-spacer, respectively with PNDIBS acceptor for efficient all-polymer solar cells. PBDB-S exhibited identical absorption spectrum to PBDB-T between 300-650 nm, while PBDBS-T displayed a 40 nm red-shift and a narrower bandgap of 1.70 eV. Both donor polymers were found to have significantly improved hole mobility (1.21×10^{-3} cm^2/Vs for PBDB-S and 9.81×10^{-4} cm^2/Vs for PBDBS-T) compared to PBDB-T. This resulted in significant enhanced PCE of 8.38% and 9.14% for inverted solar cells of PBDB-S:PNDIBS and PBDBS-T:PNDIBS respectively, compared to 8.08% of PBDB-T:PNDIBS with J_{sc} values of 17.51 mA/cm^2 and 18.38 mA/cm^2. Encouragingly, it was also found employing a conventional device architecture with PFN-Br as electron transport

layer (ETL) led to further improvements in PCE of respective devices to 9.47% for PBDBS-T:PNDIBS through the improvement the fill factors (FF) from 0.61 for PBDB-T:PNDIBS to 0.63 for PBDBS-T:PNDIBS. The deviations in photovoltaic properties may be attributed subtle differences in blend crystallization kinetics, photophysics and charge transport, reiterating the importance of synergistic focus on molecular design and device active-layer processing to control device morphology.

2.2. Experimental Section.

Synthesis. The donor copolymer PBDB-T (M_n = 57kDa, PDI = 1.90) was purchased from Brilliant Matters Organic Electronics (Quebec, Canada) and used as received, while PNDIBS acceptor copolymer was synthesised previously synthesised in our lab.[63] The detailed schematic pathways used to prepare the copolymer donors PBDB-S and PBDBS-T are represented by Scheme 1 in the Supplementary Material based on procedures suggested in other reports.[54,64,65]

Cyclic Voltammetry. Cyclic voltammetry (CV) experiments were done on an EG&G Princeton Applied Research potentiostat/galvanostat (model 273A). A three-electrode cell was used, using platinum wire electrodes as both counter and working electrodes. Ag/Ag^+ (Ag in 0.01 M $AgNO_3$ solution) was used as a reference electrode. The films of the polymer were coated onto the Pt wires by dipping the wires into polymer solutions of the polymers (PBDB-T, PBDB-S, PBDBS-T and PNDIBS) and drying the coated films at 25 °C. All the CV measurements were carried out in 0.1 M tetrabutylammonium hexafluorophosphate (Bu_4NPF_6) electrolyte solution in acetonitrile at a scan rate of 50 mV/s. The reduction and oxidation potentials were referenced to the Fc/Fc^+ couple by using ferrocene as an internal standard. The LUMO and HOMO energy levels were estimated using a ferrocene value of −4.8 eV with respect to the vacuum level.

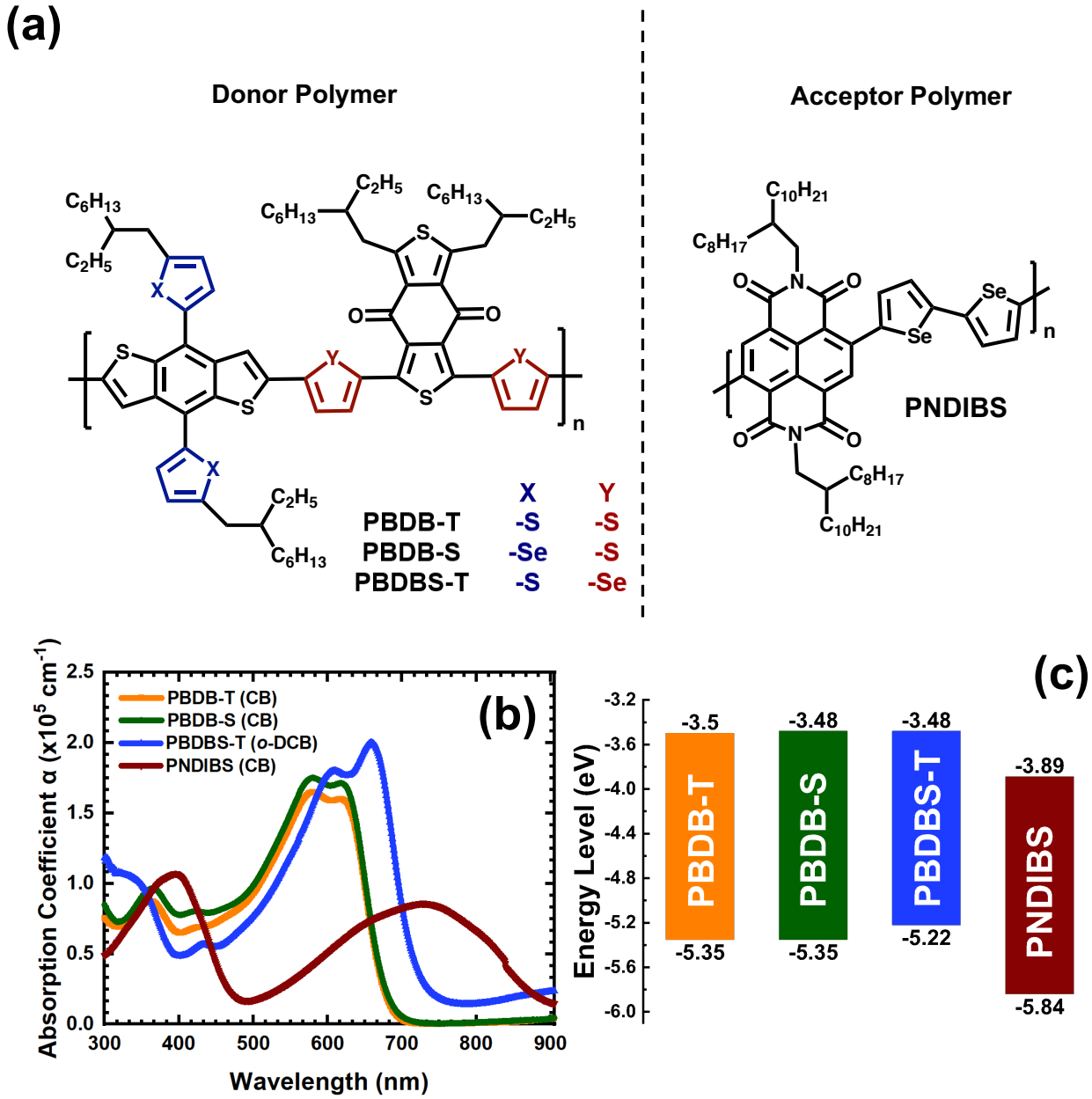

Figure 3. (a) Molecular structures of donor polymers PBDB-T, PBDB-S and PBDBS-T and acceptor polymer PNDIBS. (b) Thin-film UV-Vis absorption spectra of donor and acceptor polymers. (c) HOMO/LUMO energy level diagrams of the donors and acceptor copolymers.

Fabrication and Characterization of All-PSCs. All-Polymer Solar Cell devices were fabricated with both inverted and conventional architectures of ITO/ZnO/PEI/Blend/MoO_3 (0.5nm)/Ag (100nm) and ITO/PEDOT:PSS/Blend/PFN-Br (5nm)/Al (100nm) respectively. ITO-coated substrates (15 Ω/square, Shanghai B. Tree Tech, Shanghai, China) were subjected to sequential cleaning in ultrasonicated baths with acetone, deionized water, and isopropyl alcohol for 30 min each, followed by drying with nitrogen gas and 10 mins of oxygen plasma cleaning. The ZnO precursor solution prepared as described in a previous report[11] was spin-coated onto the ITO substrate at 5000rpm and annealed at 250 °C to obtain a ZnO thin film of c.a. 30nm. A 0.05% (wt /wt) solution of Polyethyleneimine (PEI) in 2-methoxyethanol solvent was spin-coated onto the ZnO layer at 2000rpm and dried at 120 °C for 10 min.

PBDB-T:PNDIBS and PBDB-S:PNDIBS blends (1:0.4 wt/wt) were prepared using Chlorobenzene (CB) as a solvent. The optimized blends involved incorporation of Diphenyl Ether (DPE, 0.5% (v/v)) to both blend solutions which were subsequently mixed and stirred overnight in a glovebox at 80 °C. Similarly, blends of PBDBS-T:PNDIBS (1:0.6 wt/wt) were prepared in 1,2-Dichlorobenzene (*o*-DCB) with 2% (v/v) 1,2,4-Trichlorobenzene (TCB) as additive. The aforementioned blends were mixed and stirred at 110 °C in a glovebox overnight. The optimized blend solutions were spin-coated at 1000 rpm for 50 s, followed by suitable pre-treatment pathway. MoO_3 (0.5 nm) and Ag (100 nm) were thermally deposited onto the active layer at a pressure of 2×10^{-6} torr. Conventional Solar Cells were fabricated using PEDOT:PSS (Clevios, VP, Al 4083, Heraeus, Germany) spin-coated on ITO substrates at 2000 rpm followed by annealing at 150 °C for 10 mins. The active layers were spin-coated onto the PEDOT:PSS layer as described above, under identical pre-treatment conditions in an Argon-filled glovebox. Subsequently, PFN-Br (0.5mg/ml in methanol solvent) was deposited on top of the active layers as an electron transport

layer to obtain a thin film of c.a. 5 nm. The top electrode, Al (100 nm) was then thermally evaporated at a pressure of 5×10^{-7} torr. All active layers were found to have a thickness of c.a. 95 ± 10 nm.

The photovoltaic cells thus prepared were tested under AM 1.5G solar illumination at 100 mW/cm^2 in ambient air by using a solar simulator (model 16S, Solar Light Co., Philadelphia, PA) with a 200 W xenon lamp power supply (model XPS 200, Solar Light Co., Philadelphia, PA) calibrated by an NREL-certified Si photodiode (model 1787-04, Hamamatsu Photonics K.K., Japan) and a HP4155A semiconductor parameter analyzer (Yokogawa Hewlett-Packard, Japan).

After the *J–V* measurements, the external quantum efficiency (EQE) spectra were measured by using a solar cell quantum efficiency measurement system (Model QEX10, PV Measurements, Inc., Boulder, CO) with a 2 mm^2 (2 mm × 1 mm) size masked incident light source and a TF Mini Super measurement apparatus for multiple devices in a single substrate. The EQE system was calibrated with a Si photodiode before measurement.

Fabrication and Characterization of SCLC Devices. Current–voltage (*J–V*) characteristics of the space-charge limited current (SCLC) devices were measured by using a HP4155A semiconductor parameter analyzer (Yokogawa Hewlett-Packard, Tokyo). The carrier mobility was deduced by fitting the *J–V* curves to the Mott–Gurney equation,

$$J = \frac{9}{8}\varepsilon_0 \varepsilon \mu \frac{V^2}{L^3}$$

where J is the current density, ε_0 is the permittivity of free space, ε is the relative permittivity, μ is the zero-field mobility, V is the applied voltage, and L is the thickness of an active layer.

The SCLC device structures for electron-only and hole-only were ITO/ZnO/PEI/Blend/PFN-Br (5 nm)/Al (100 nm) and ITO/PEDOT:PSS/Blend/MoO_3 (7.5 nm)/Ag (100 nm), respectively. Each active layer of both neat and blend films was processed at the optimized All-PSC device conditions as described above and spin-coated at 1000 rpm for 50 s and followed the optimal pre-treatment for the respective donor used in blend. All active layers prepared were c.a. 150 ± 20 nm thick.

AFM Imaging. Atomic force microscopic (AFM) characterization of the surface morphology was done on the active layers of the actual polymer solar cells, used in the photovoltaic measurements, by using a Bruker Dimension scanning probe microscope (SPM) system. The approximate domain or grain sizes and root-mean-square surface roughness (R_q) were computed using Gwyddion software.

X-Ray Diffraction. XRD patterns were collected on a Bruker D8 Discover Microfocus diffractometer with Cu Kα beam (1.54 Å) as the X-ray source. Neat films of donor polymer (PBDB-T, PBDB-S, PBDBS-T) films were prepared by drop-casting of highly concentrated solutions in Chlorobenzene and 1,2-Dichlorobenzene onto glass substrates to obtain films of thickness c.a. 330 ± 30nm and treated under the optimized conditions as discussed in the photovoltaic performance section. XRD patterns were recorded using θ/2θ scans, the incident beam passed through 0.3 mm collimator and pinhole, and the incident angle between the beam and sample was fixed at 1°. The 2D-diffraction images were captured using a PILATLUS3R 100-A area detector placed at 16 cm from the sample. The 1-D data (2θ vs intensity) were processed by integrating the 2-D images using EVA software. The *d*-spacing values were found using Bragg's Law. The full-width half maxima FWHM data in degrees for the respective neat and blend films

was generated by obtaining the Gaussian fit of the d_{100} peak in Originlab software. The mean crystallite domain sizes (L_c) were calculated using the Scherrer equation denoted as follows: $L_C = \frac{k*\lambda}{\beta*cos\theta_{(100)}}$, where k is a shape factor (assumed to be 0.9), λ the wavelength of Cu Kα beam (1.54 Å), β the FWHM in radians and $\theta_{(100)}$ is the peak position in degrees.

2.3. Optical and electronic properties.

The ultra-violet visible (UV-Vis) optical absorption spectra of PBDB-T, PBDB-S, PBDBS-T and PNDIBS thin films on glass are displayed in Figure 3b. Thin films of PBDB-T and PBDB-S were cast from Chlorobenzene, while 1,2-Dichlorobenzene was used as a processing solvent for PBDBS-T polymeric films. The absorption spectrum of PBDB-S film displays absorption bands in the wavelength range of 300 nm to 700 nm, similar to its thiophene equivalent, PBDB-T. The two respective polymers PBDB-T and PBDB-S display two characteristic peaks at 566 nm and 625 nm, representing π-π* transition and interchain π-π* transition due to π-π stacking of the backbones respectively. The absorption onset of PBDB-T was found to be at 688 nm, while that of PBDB-S was at 697 nm, corresponding to an absorption edge optical band gap (E_g^{opt}) of 1.80 eV and 1.78 eV respectively. On the other hand, PBDBS-T donor displayed similar red shifted absorption peaks at approximately 600 nm and 664 nm in contrast to the aforementioned donors with a significantly pronounced vibronic absorption.[54] The enhanced main peaks of PBDBS-T at 664 nm compared to those of PBDB-T and PBDB-S at 625 nm are also indicative of strong intermolecular π–π stacking post molecular modification with selenophene as π-spacer. Consequently, the absorption onset shifted to 729 nm, corresponding to E_g^{opt} value of 1.70 eV. PNDIBS acceptor also exhibits two peaks with π-π* and ICT peaks at 394nm and 716nm. The absorption profiles were also found to complement that of the acceptor, PNDIBS, used in this

study which had E_g^{opt} of 1.40 eV.[37] All three donors used displayed high film absorption coefficients (α) with PBDB-T having an α of 1.6×10^5 cm^{-1}, PBDB-S with 1.73×10^5 cm^{-1} and PBDBS-T with 2×10^5 cm^{-1}. The superior electron donating nature of selenophene compared to thiophene by virtue of larger and looser outermost electron cloud has led to the enrichment of the electron density of the BDT backbone, thus leading to superior optical properties of PBDB-S and PBDBS-T and a narrower bandgap for PBDBS-T.

The energy levels of the donor and acceptor component polymers used were measured using cyclic voltammetry. The representative redox voltammograms are shown in Figure S1 and the electronic highest occupied molecular orbital (HOMO) and lowest unoccupied molecular orbital (LUMO) levels evaluated using the onset of the oxidation and reduction potentials are illustrated by Figure 3c, Figure S1 and Table S1. The HOMO levels were calculated to be -5.35, -5.35 and -5.22 eV for PBDB-T, PBDB-S and PBDBS-T respectively, while the LUMO energy levels were approximately the same across the donor copolymers at -3.50, -3.48 and -3.48 eV respectively. Selenophene substitution on the conjugated side chain led to little to no change in the LUMO, while the HOMO has been slightly upshifted by c.a. -0.13 eV in the case of Selenophene π-spacer, in accord to trends observed previously.[66] This is ascribed to the stronger electron-donating nature of Se. Additionally, the HOMO of all three donor polymers are sufficiently greater than that of PNDIBS acceptor copolymer, as seen in Figure 3c., suggesting that there is sufficient driving force for exciton photogeneration and efficient charge separation.

2.4. Photovoltaic Performance.

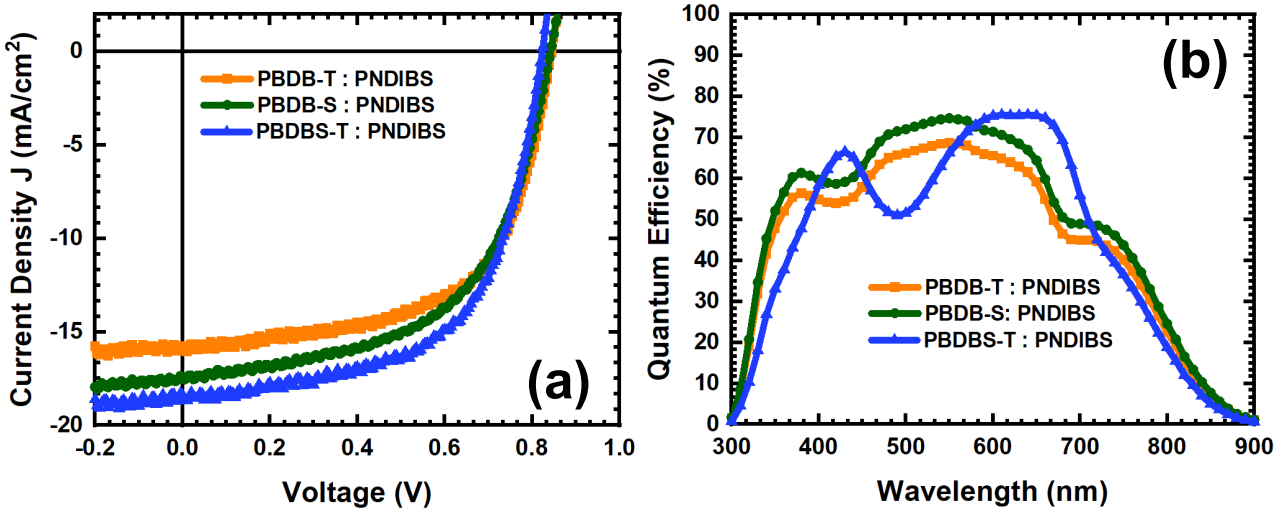

Figure 4. Current density (*J*) - Voltage (*V*) characteristics under AM 1.5G illumination (a) and External quantum efficiency (EQE) spectra (b) for optimized blends of PBDB-T:PNDIBS, PBDB-S:PNDIBS and PBDBS-T:PNDIBS based inverted All-Polymer Solar Cells.

Inverted Solar Cells with the architecture ITO/ZnO/PEI/Blend/MoO_3/Ag were fabricated to evaluate the photovoltaic performance of the binary blends composed of PBDB-T:PNDIBS, PBDB-S:PNDIBS and PBDBS-T:PNDIBS. The blend active layer's composition and processing conditions were systematically optimized by investigating the effect of different donor: acceptor (D:A) ratio, thermal annealing at different temperatures, controlling solvent evaporation rate through film aging and incorporation of processing additives on device performance. Details pertaining to the optimization process are outlined by Tables S2-S6 along with the photovoltaic parameters including the short-circuit current (J_{sc}), open circuit voltage (V_{oc}), fill factor (FF) and power conversion efficiency (PCE %). Representative current density-voltage plots (*J-V*) are depicted by Figures S4-S8.

Similar to a prior report, PBDB-T:PNDIBS blends were optimized by casting thin films from Chlorobenzene (CB) at a D:A ratio of 1:0.4 (wt/wt) with 0.5% Diphenyl Ether (DPE) solvent processing additive followed by thermal annealing at 130 °C for 10 minutes in an Argon filled glovebox.[38,63] The optimal processing conditions for PBDB-S:PNDIBS blends include a D:A ratio of 1:0.4 (wt/wt) with 0.5% DPE in CB, with thermal annealing of the cast thin films at 175 °C. However, as a result of the poor solubility of PBDBS-T in CB, 1,2-Dichlorobenzene (*o*-DCB) was employed as a solvent for the PBDBS-T:PNDIBS devices. The devices were fabricated using active layers with a D:A ratio of 1:0.6 wt/wt PBDBS-T:PNDIBS. *o*-DCB solutions were spin coated at 1000 rpm for 50 s followed by drying of the obtained wet films through aging in the glovebox for 3 hrs. The photovoltaic parameters of the devices thus optimized are summarized as follows by Table 1 and Figure 4a.

It was found that the parameters vary quite significantly with the pre-processing conditions, depending on the choice of donors and site of selenophene substitution. Firstly, the systems with selenophene substituted on their backbones (PBDBS-T:PNDIBS) were optimized at a D:A ratio of 1:0.6 as opposed to PBDB-T:PNDIBS and PBDB-S:PNDIBS which were optimized at D:A ratio of 1:0.4. This is consistent with the slightly enhanced absorption coefficient of PBDBS-T in contrast to the latter donors.

Inverted All-Polymer Solar Cells were fabricated from PBDB-S:PNDIBS blends with a D:A ratio of 1:0.4 (wt/wt) and displayed starkly divergent photovoltaic properties depending on the nature of processing; The devices aged in the glovebox were found to have an average PCE of 6.71% with a J_{sc} of 15.01 mA/cm^2, a V_{oc} of 0.865 V, and a FF of 0.517 while the thermally annealed devices displayed a significantly improved PCE of PCE of 7.69% with a J_{sc} of 16.77 mA/cm^2, a

V_{oc} of 0.845 V, and a FF of 0.549. Processing additives were systematically screened to improve the nanostructure and modulate the extent of phase separation. It was found that the incorporation of 0.5% DPE (v/v) to the Chlorobenzene blend led to improved performance of the thermally annealed devices through significant enhancement of J_{sc} and FF. V_{oc} was unaffected at 0.845 V, while the J_{sc} had improved to 17.51 mA/cm^2 and the FF increased marginally to 0.563. Thus, the optimized PBDB-S:PNDIBS devices displayed an average PCE of 8.38%. (Table 1)

The photovoltaic properties of PBDBS-T:PNDIBS devices with a D:A ratio of (1:0.6 wt/wt) in *o*-DCB solvent were found to be enhanced compared to those of PBDB-S:PNDIBS devices. The devices subjected to film aging exhibited an average PCE of 8.44% with a J_{sc} of 17.62 mA/cm^2, a V_{oc} of 0.815 V, and a FF of 0.582. The V_{oc} of the aforementioned system was found to be lower than those exhibited by PBDB-S:PNDIBS devices, as a result of the upshifted HOMO levels of PBDBS-T. A similar effect caused by the selenophene substitution on the backbone of the BDT unit of a different polymeric system has been reported previously.[58] Surprisingly, the thermally annealed devices (Optimized at 150 °C) displayed reduced performance compared to the aged counterpart with a PCE of 7.67% with a J_{sc} of 17.1 mA/cm^2, a V_{oc} of 0.78 V, and a FF of 0.571 in stark contrast to the trend exhibited by PBDB-S:PNDIBS devices. While the average values of J_{sc} and FF are comparable to an extent, the V_{oc} was found to have reduced significantly (c.a. 0.035 V); a trend that has been noted previously in other crystalline polymeric systems that exhibit strong aggregation properties and aggregation limited morphology.[25,67–69]

Table 1. Summary of photovoltaic properties of inverted solar cell devices of 1:0.4 wt/wt PBDB-T:PNDIBS, 1:0.4 wt/wt PBDB-S:PNDIBS and 1:0.6 wt/wt PBDBS-T:PNDIBS subject to different pre-treatment conditions

Donor Polymer	Additive used	Condition	J_{sc} (mA/cm^2)	V_{oc} (V)	FF	PCE_{ave} (%)
PBDB-T		Aged (3hrs)	14.32	0.870	0.522	6.47 (±0.32)
PBDB-T		Annealed (130 °C)	15.11	0.865	0.581	7.45 (±0.24)
PBDB-T	DPE (0.5%)	Annealed (130 °C)	15.76	0.855	0.600	8.08 (±0.1)
PBDB-S		Aged (3hrs)	15.01	0.865	0.517	6.71 (±0.18)
PBDB-S		Annealed (175 °C)	16.77	0.845	0.549	7.69 (±0.19)
PBDB-S	DPE (0.5%)	Annealed (175 °C)	17.51	0.845	0.563	8.38 (±0.23)
PBDBS-T		Aged (3hrs)	17.62	0.815	0.582	8.44 (±0.33)
PBDBS-T		Annealed (150 °C)	17.10	0.780	0.571	7.67 (±0.29)
PBDBS-T	TCB (2%)	Aged (3hrs)	18.38	0.825	0.607	9.14 (±0.18)

It was also observed that the additives previously investigated for PBDB-S:PNDIBS had a detrimental effect on the device performance in blends based on PBDBS-T:PNDIBS, as elucidated by Figure S6 and Table S4. This may be a consequence of poor solubility of PBDBS-T in conventional solvents such as 2-MeTHF, THF, CB etc. and additives (c.a. <3 mg/ml in CB) due to the presence of selenophene-spacer in the backbone. Thus, the differential aggregation rates

required to suppress aggregation and enable optimal domain sizes[70] was not achieved due to the absence of preferential solubility of donor phase, characteristic of other reported donor:acceptor blends with incorporated processing additive. As a result, 1,2,4-Trichlorobenzene (TCB) was investigated as an alternative, owing to the high solubility of PBDBS-T in the same.

An average PCE of 9.14% with a J_{sc} of 18.38 mA/cm^2, V_{oc} of 0.825 V and FF of 0.607 was obtained by film aging PBDBS-T:PNDIBS devices after incorporating 2% TCB. (Figure S8, Table S6) The mechanism of enhancement of aged all-PSCs subjected to relatively slower solvent evaporation rate enabling modulation rate and nanomorphology of the active layer has been suggested in literature previously.[25]

PBDB-T:PNDIBS devices were also fabricated to serve as a standard for comparison to contrast between unsubstituted/thiophene substituted donor and selenophene substituted donors. PBDB-T:PNDIBS devices were found to be optimized at a D:A ratio of 1:0.4 wt/wt followed by thermal annealing at 130 °C with 0.5% DPE with a PCE of 8.08%, J_{sc} of 15.76 mA/cm^2, V_{oc} of 0.845 V and FF of 0.60. The observation that thermal annealing of PBDB-T:PNDIBS devices elicit better PCE has already been reported and investigated extensively in a prior report.[37]

Encouragingly, it was also found that improved PCE values may be obtained using conventional device architecture with ITO/PEDOT:PSS/Active layer/PFN-Br/Al across all three blend systems, notably because of fill factor enhancement. (Figure S11, Table S9) This further boosted the PCEs of the all-PSCs to 8.38%, 8.81% and 9.47% with FF values of 0.614, 0.592 and 0.635 for PBDB-T:PNDIBS, PBDB-S:PNDIBS and PBDBS-T:PNDIBS devices respectively, while the J_{sc} values were largely unchanged. This suggests the possibility of interface engineering of the electron transport layer (ETL) of both conventional and inverted solar cells to achieve

improved electron collection. As revealed by the SCLC results (*Vide infra)*, the electron mobilities of the blends lag quite significantly behind the respective hole mobilities. It is possible that by using superior ETLs with greater conductivity, improved values of FF may be obtained by increase overall electron mobility, facilitating a balance of charge transport. A similar effect has been achieved previously through the intercalation of alkali metals (Li) or Al in the defects of zinc oxide electron transport layer in case inverted fullerene-based solar cells with a different active layer composition.[71–73] PCEs of 9.47% were obtained for blends composed of PBDBS-T:PNDIBS with a J_{sc} of 18.26 mA/cm^2, V_{oc} of 0.825 V and FF of 0.635. These values are among the higher efficiencies for all-PSC devices.

2.5. External Quantum Efficiency.

The External Quantum Efficiency (EQE) spectra of optimized inverted solar cell devices fabricated from PBDB-T:PNDIBS, PBDB-S:PNDIBS and PBDBS-T:PNDIBS are depicted in Figure 4b. All blends feature a wide absorption window of c.a. 885 nm to 310 nm. As the photocurrent generated in the 700-885 nm and 300-450 nm bracket is a result of photoinduced hole transfer to the PNDIBS acceptor polymer, it is clear that the photocurrent harvested in the 450-720 nm region is due to the efficient photoinduced electron transport of the donor polymers. The EQE spectra displayed by PBDB-T:PNDIBS and PBDB-S:PNDIBS systems are largely similar, encompassing similar wavelengths with identical line shape. However, it should be noted that the peak EQE of PBDB-S is significantly enhanced at 74.6% at 550 nm, compared to PBDB-T devices at 68.8% at 560 nm. This is consistent with the previously discussed increase in J_{sc} as shown in the photovoltaic data (Figure 4a, Table 1) and the spectral overlap between the two donors as demonstrated by the UV-Vis spectroscopy (Figure 3b). On the other hand, the EQE of

PBDBS-T based devices shows a prominent decrease in the 420-520 nm region and increased photon harvesting in the 600-700 nm range as compared to PBDB-T:PNDIBS and PBDB-S:PNDIBS systems with a maximum quantum efficiency of 75.5% corresponding to 640 nm. The red-shifted absorption as a result of selenophene substitution on the backbone of PBDBS-T donors by c.a. 40 nm has resulted in short-circuit currents that exceed those of devices based on PBDB-T:PNDIBS and PBDB-S:PNDIBS. The EQE spectra originating from the short-wavelength absorption by PNDIBS is also found to be slightly enhanced in PBDBS-T:PNDIBS devices, thereby implying that selenophene π-spacers facilitate greater photonic conversion by PNDIBS acceptor. These inferences are consistent with the normalised UV-Vis absorption spectra of the blend devices in Figure S3. J_{sc} values obtained through the integration of the EQE spectra are found to collaborate well with J-V data and are within a 5% mismatch.

Several conclusions may be drawn pertaining to the photovoltaic device data and EQE spectral data presented above that are relevant towards the further development of All-PSCs. Firstly, selenophene substitution in place of thiophene on the different positions of benzodithiophene (BDT) building block has been investigated and demonstrated to be a viable strategy to improve the performance of All-Polymer Solar Cells in conjunction with a high-mobility selenophene containing acceptor, PNDIBS. Interestingly, alkyl-selenophene side chains did not facilitate the desired increase in photovoltaic performance as a result of reduced FF. However, the presented results clearly warrant that the substitution of a selenophene moiety on the BDT backbone (π-spacer) is beneficial to photovoltaic performance by virtue of red-shifted absorption of PBDBS-T based All-PSCs and improved J_{sc}. It is possible that the larger atomic radius of selenium causes alkyl-selenophene side chains on BDT donors interfere with

intermolecular interaction,[74,75] while the presence of selenophene as π-spacer enhances planarity and conjugation length.

Another point of interest arises from the observation that the pathways (e.g. slow solvent evaporation as opposed to rapid annealing) that lead to optimal performance varied depending on the location of the moiety; ie. Thermal annealing for PBDB-T:PNDIBS, PBDB-S:PNDIBS and aging for PBDBS-T:PNDIBS. This is believed to arise from differential effects in crystallinity post selenophene modification and indicates differences in the film forming and crystallization kinetics between PBDB-S and PBDBS-T. The metallic nature of selenium leads to noticeably increased crystallinity when incorporated in the polymeric backbone, which is desirable for charge transport.[76,77] The increased crystallinity of PBDBS-T is corroborated by the stark difference in V_{oc} between aged and annealed PBDBS-T:PNDIBS devices, as a result of density of states broadening caused by thermal-annealing induced disorder and recombination.[67] This partially explains how slow evaporation of *o*-DCB led to heightened PCE values. This hypothesis is corroborated by X-Ray Diffraction results. (*Vide infra*)

Lastly, as the number of studies of All-Polymer Solar Cells containing selenophene based donors is limited, there lies a great deal of potential towards improvement of notably the FF, which lags behind quite significantly behind other state-of-the art All-PSCs.[32,34,35,67,78] It is worth mentioning that the substitution of selenophene in the BDT backbone lead to a reduction in solubility with low-boiling solvents, and that limits the extent to which crucial features such as domain purity may be manipulated using say, cosolvents with low boiling points to form purer and larger polymer domains.[36,38] Some considerations towards the improvement of solubility and FF can include the rational selection of side-chains and inclusion of random copolymeric units.

2.6. Exciton Dissociation and Charge Recombination.

The photoinduced charge carrier generation and collection was evaluated in the respective blends by investigating the photocurrent density J_{ph} ($J_{ph} = J_L - J_D$) as a function of effective voltage V_{eff} ($V_{eff} = V_{bi} - V_a$). J_L and J_D denote the current densities under illuminated and dark conditions, while V_{bi} and V_a denote the built-in potential where $J_{ph} = 0$ and applied voltage, respectively. The J_{ph} value was found to saturate at fairly high V_{eff} values ($V_{eff} > 2V$) for all devices fabricated. Based on Figure 5., it may be concluded that the effective voltage is large enough to extract almost all free charges photogenerated to the electrodes at the saturation point. The saturation photocurrent

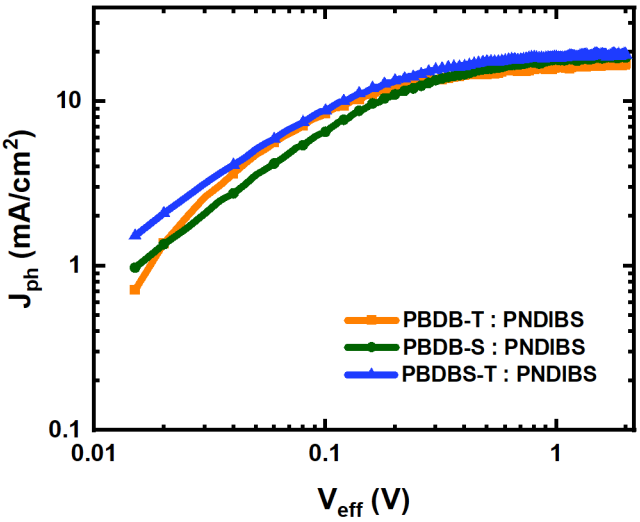

Figure 5. Photocurrent density J_{ph} – effective voltage V_{eff} curves for the optimized PBDB-T:PNDIBS, PBDB-S:PNDIBS, PBDBS-T:PNDIBS blend devices.

(J_{sat}) values in this regime were found to be 16.6 mA/cm^2 for PBDB-T, 18.6 mA/cm^2 for PBDB-S and 19.1 mA/cm^2 for PBDBS-T based systems. Thus, the collection probability values $P(E, T)$ under short-circuit conditions were evaluated by $P(E, T) = J_{sc}/J_{sat}$. $P(E, T)$ was calculated to be 94.5% for PBDB-T:PNDIBS, 94% for PBDB-S:PNDIBS and 95.2% for PBDBS-T:PNDIBS. The collection probability of PBDB-T:PNDIBS devices was found to be slighter superior to those of

PBDB-S:PNDIBS, which is reflected by the reduced FF of PBDB-S devices. Similarly, maximum photoinduced carrier generation rate G_{max} was estimated using the saturation photocurrent density by $G_{max} = J_{sat}/ qL$, where q represents the elementary coulombic charge and L, the thickness of the fabricated active layers. G_{max} values of 1.04×10^{28}, 1.16×10^{28} and 1.19×10^{28} $m^{-3} s^{-1}$ were obtained for PBDB-T, PBDB-S and PBDBS-T donors, respectively indicative of good exciton dissociation rates. Based on the charge collection probability and the saturation photocurrent density values summarized in Table S10, it is clear that PBDBS-T:PNDIBS devices feature more efficient charge collection processes, light absorption and exciton dissociation. This also corroborates with the previously discussed photovoltaic properties and account for the superior J_{sc} and FF values.

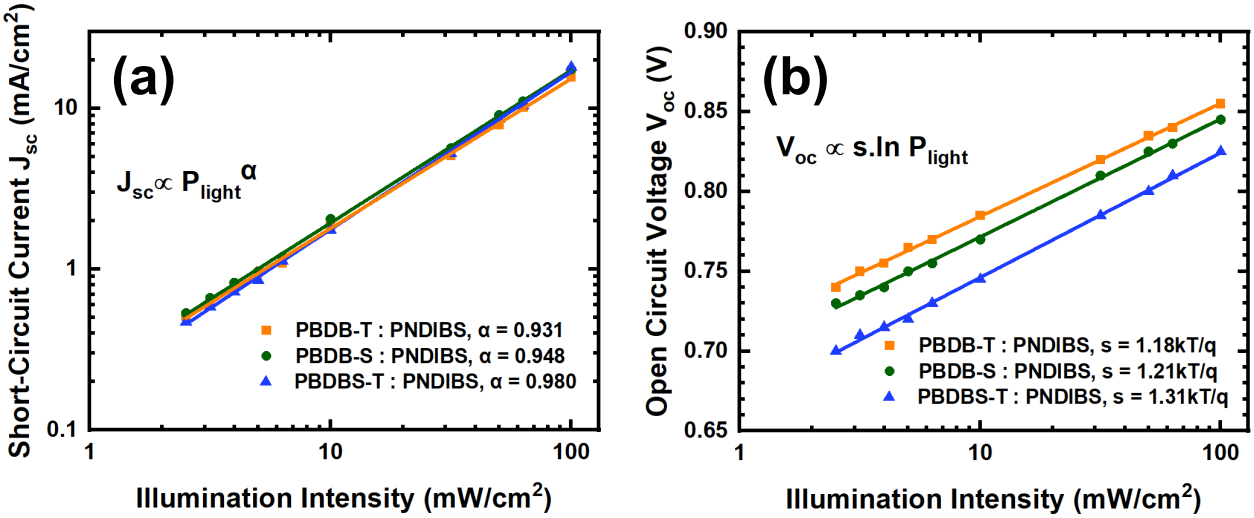

Figure 6. J_{sc} dependence on illumination intensity of incident light (a) and V_{oc} dependence of illumination intensity of incident light (b) for optimized blend devices of PBDB-T:PNDIBS, PBDB-S:PNDIBS and PBDBS-T:PNDIBS respectively.

Short-circuit current as a function of illumination intensity (J_{sc} vs P_{light}) was measured to gain insight on the charge recombination kinetics of the All-PSCs and the effect of selenophene substitution. As expected, the J_{sc} followed the power-law dependence on P_{light} ($J_{sc} \propto P_{light}^{\alpha}$), where a linear correlation signifies the complete extraction of all charge carriers prior to recombination. The fitted plots illustrated by Figure 6a. resulted in comparable α values of 0.93 and 0.95 values for PBDB-T:PNDIBS and PBDB-S:PNDIBS, suggesting the dominance of bimolecular recombination, partly explaining the relatively low J_{sc} of PBDB-T:PNDIBS systems and low FF of PBDB-S:PNDIBS. PBDBS-T: PNDIBS blends displayed suppressed bimolecular recombination with α of 0.98.

The relationship between V_{oc} and P_{light} is represented as $V_{oc} \propto s \times \ln (P_{light})$. The proportionality constant and slope s usually varies between 1 and 2, suggesting the presence of dominant biomolecular recombination (s = 1 kT/q) or trap-assisted recombination (s = 2 kT/q) respectively. As exemplified by Figure 6b., PBDB-T and PBDB-S based devices have a gentle slope and are governed by bimolecular recombination (s = 1.18 kT/q and s = 1.21 kT/q respectively), while PBDBS-T:PNDIBS devices display relatively suppressed bimolecular recombination (s = 1.31 kT/q). The above results corroborate well with the obtained photovoltaic data for optimized devices. Indeed, the devices based PBDBS-T displayed a superior FF, particularly using the conventional solar cell architecture by virtue of their suppressed bimolecular recombination.

2.7. Charge Transport Properties.

The bulk charge transport properties of the neat donor films and blends with PNDIBS acceptor under their respective optimized conditions have been characterized by Space-Charge

Limited Current (SCLC) to further probe the photovoltaic properties and develop insights pertaining to trends exhibited by J_{sc} and FF. The zero-effect mobilities were extracted from the generated *J-V* curves under dark condition by fitting them to the Mott-Gurney Equation. The following architectures were used to fabricate single-charge carrier devices: ITO/PEDOT:PSS/Blend/MoO_3 (7.5 nm)/Ag (100 nm) for hole-only devices and ITO/ZnO/PEI/Blend/PFN-Br (5 nm)/Al (100nm) for electron-only devices. The *J-V* plots and their curve-fitted lines for neat donor films and blend films are shown in Figures S12 and S13 and the charge carrier mobilities have been compiled in Table 2.

The neat films of unsubstituted donor PBDB-T show a hole mobility (μ_h) of 4.05×10^{-4} cm^2/Vs, which is in agreement with values reported in literature. However, both selenophene substituted donors PBDB-S and PBDBS-T revealed substantially higher μ_h values of 1.21×10^{-3} cm^2/Vs and 9.81×10^{-4} cm^2/Vs respectively. The charge mobility enhancement upon selenophene substitution as a result of greater polarizability of Se compared to S, favourable interchain Se-Se interactions, improved crystallinity and greater face-on tendency has already been reported previously. The three-fold increase in magnitude of μ_h reveals the positive effect of selenophene substitution on field-effect mobilities and speaks well of the potential of the synthesized donors in Polymer Solar Cells when paired with high mobility acceptors.

Table 2. SCLC mobilities of neat films of PBDB-T, PBDB-S and PBDBS-T and blend films of PBDB-T:PNDIBS, PBDB-S:PNDIBS and PBDBS-T:PNDIBS. All devices were fabricated under the optimal processing conditions.

Film composition	μ_h (cm^2/Vs)	μ_e (cm^2/Vs)	μ_h / μ_e
PBDB-T (Neat)	4.05×10^{-4}	-	-
PBDB-T:PNDIBS	3.84×10^{-4}	1.04×10^{-4}	3.7
PBDB-S (Neat)	1.21×10^{-3}	-	-
PBDB-S:PNDIBS	1.14×10^{-3}	3.34×10^{-4}	3.4
PBDBS-T (Neat)	9.81×10^{-4}	-	-
PBDBS-T:PNDIBS	8.789×10^{-4}	5.13×10^{-4}	1.7

With respect to the blend devices, the bulk hole mobilities were found to be quite similar to those of the neat donor films at 3.84×10^{-4} cm^2/Vs for PBDB-T:PNDIBS, 1.14×10^{-3} cm^2/Vs for PBDB-S:PNDIBS and 8.78×10^{-4} cm^2/Vs for PBDBS-T:PNDIBS. However, differing values of electron mobility μ_e were observed between the blends. In contrast to the μ_e of 1.04×10^{-4} cm^2/Vs seen in PBDB-T:PNDIBS blends, a threefold increase to 3.34×10^{-4} cm^2/Vs in PBDB-S:PNDIBS and an enhancement of approximately 5 times at 5.13×10^{-4} cm^2/Vs in PBDBS-T:PNDIBS were observed, accounting for the improved photovoltaic performances. It is worth noting that while the improved hole mobilities in PBDB-S:PNDIBS active layers warrant the increase in J_{sc}, the charge transport remains quite unbalanced at a μ_h / μ_e of 3.413, which is comparable to PBDB-T:PNDIBS at 3.692. It is known that unbalanced μ_h / μ_e results in charge recombination in all-PSCs and may lead to deterioration of fill factors. Therefore, it is possible

that the relatively lower fill factors exhibited by PBDB-S devices are owing to sub-optimal morphology in blend.

PBDBS-T:PNDIBS based devices feature relatively more balanced charge transport properties at μ_h / μ_e of 1.713. Thus, the synergistic effect of increased hole mobility and red-shifted absorption of PBDBS-T as elucidated by EQE and UV-Vis results and relatively balanced charge transport with PNDIBS acceptor have resulted in enhanced J_{sc} and FF. The greater values of μ_e also suggests a more optimal morphology for PBDBS-T:PNDIBS blends.

2.8. Atomic Force Microscopy.

Atomic force microscopy imaging (AFM) was used to characterize PBDB-T:PNDIBS, PBDB-S:PNDIBS and PBDBS-T:PNDIBS blend films to generate insights on surface morphology. While all three blend devices displayed distinct needle-like features, clear differences were observed in terms of domain sizes and roughness. The optimized devices of PBDBS-:PNDIBS possessed a relatively rougher surface with greater root-mean-square roughness (R_q) values (R_q = 1.673 ± 0.196 nm) in comparison to that of PBDB-T:PNDIBS (R_q = 1.56 ± 0.279 nm) and PBDB-S:PNDIBS (R_q = 1.23 ± 0.288 nm) with a more suitable fiber structure and more obvious extent of phase separation with larger domains in the range of 20-30 nm, as seen in Figures 7a, 7b and 7c. The smoother surface of PBDB-S:PNDIBS indicates the possibility of molecular intermixing between donor and acceptor polymeric phases, and a lower degree of phase separation for PBDB-S:PNDIBS compared to their pure thiophene equivalents. Furthermore, PBDB-S:PNDIBS blends exhibit marginally smaller grains than the other two blends, that display comparable domain sizes in the range of 20-30 nm with a lesser extent of phase separation compared to the former devices. In contrast, PBDBS-T:PNDIBS blends display a more suitable

fiber structure with increase roughness and more obvious phase separation, which serves to reduce bimolecular recombination losses.

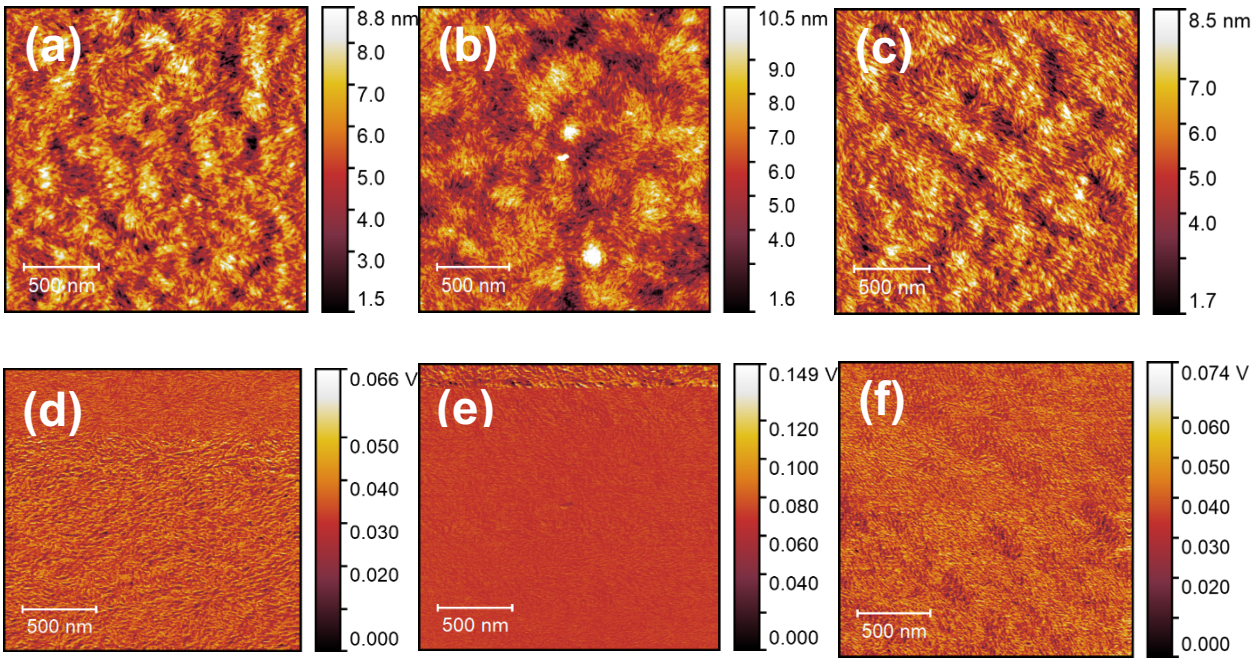

Figure 7. Atomic force microscopy (AFM) height (a, b, c) and phase (d, e, f) images (2 µm x 2 µm) of all-PSC blend devices based on PBDB-T:PNDIBS, PBDB-S:PNDIBS and PBDBS-T:PNDIBS processed under the optimized conditions with lateral scale bars of 500 nm

2.9. X-Ray Diffraction.

An understanding of intermolecular ordering and crystallinity is essential for the design of high-performance all-PSCs. Thus, X-ray Diffraction was performed on thin films of both the neat p-type polymers and polymers blended with PNDIBS acceptor to verify the presence of any differences in crystallinity and to obtain a ballpark of the crystallite sizes. All three donor polymers and blend films displayed a prominent lamellar (100) peak between 2-7° and a (010) π-π stacking peak between 20-30°. The (100) peaks of PBDB-T, PBDB-S and PBDBS-T lie at a 2θ value of 4.44, 4.4 and 4.36 respectively, corresponding to a lamellar-stacking distance of 19.85, 20.03 and

20.21Å. Mean crystallite domain sizes (L_c) of 5.48nm, 4.38nm and 6.52nm were observed for the neat films of PBDB-T, PBDB-S and PBDBS-T respectively (Figure S14 and Table S11), indicating the subtle changes in crystallinity. Incorporation of Se on the side-chain has resulted in a decrease in crystallite size compared to PBDB-T as in the case of PBDB-S, whereas PBDBS-T displays greater crystallinity and longer coherence lengths, as elucidated by the heightened d_{100} values. Whereas, the values of d_{010} of the three donor polymers were found to be almost identical, revealing that selenophene substitution has a weak effect of the π-π stacking lengths.

Likewise, L_c values of 6.82nm, 5.87nm and 7.86nm were obtained for blend systems of PBDB-T:PNDIBS, PBDB-S:PNDIBS and PBDBS-T:PNDIBS respectively. (Figure S15 and Table S11) It is worth noting that the mean crystallite sizes of the blends are significantly reduced compared to the L_c values of neat PNDIBS acceptor, at c.a. 12.4nm.[37] PBDB-S:PNDIBS blends displayed lower values for lamellar packing (21.42Å), suggesting that the conjugated selenophene side-chain may be restraining the intermolecular crystallization in the bulk. PBDBS-T:PNDIBS blend films are shown to possess longer coherence lengths (21.63Å) and larger crystallite sizes, which are beneficial for the improvement of J_{sc} and FF.

The AFM and XRD data in tandem suggest that there is a suppression in phase separation induced by the presence of selenophene in the conjugated side chain position of the BDT block, leading to the formation of smaller and amorphous domains. As a result, there is significant intermixing between the phases. While intermixing of donor and acceptor domains is certainly beneficial due to increased D/A interfacial area to facilitate lower rates of monomolecular recombination, they are detrimental to charge transport and often promote bimolecular recombination and lower exciton dissociation rates, as observed in Figure 5 and Figure 6a. In

contrast, PBDBS-T:PNDIBS blends feature optimal phase separation, with moderate size and crystalline domains, that facilitate suppressed bimolecular recombination and balanced charge transport as evidenced by the SCLC results.[30] Thus, these results highlight that the bulk crystallinity of the donor polymer when paired with an acceptor polymer is a critical factor in regulating the photovoltaic efficiency and endows blend compatibility, and that it is a factor to be taken into account during rational molecular design to construct state-of-the-art PSCs.

2.10. Conclusions.

Two new conjugated donor copolymers, PBDB-S and PBDBS-T, were designed and synthesised based on PBDB-T by inserting selenophene moieties on the conjugated side chain of BDT building block and π-spacer of PBDB-T D-A copolymer respectively. The two polymers were found to have wide bandgaps of 1.78 eV and 1.70 eV with PBDBS-T having a narrower bandgap than the reference PBDB-T (1.80 eV). The SCLC results reveal that both polymers had significantly enhanced hole mobilities compared to PBDB-T. All-PSCs fabricated based on PBDBS-T:PNDIBS demonstrated a superior PCE of 9.14% with a high J_{sc} of 18.38mA/cm^2 among the three donors compared, as it fully benefited from red-shifted absorption, higher absorption coefficient, longer lamellar stacking, bulk crystallinity and suitable phase-separated morphology. These results indicate that the insertion of a selenophene π-spacer to a D-A polymeric backbone has a strong effect of the photovoltaic properties and photophysics of all-polymer solar cells to further guide molecular design.

Chapter 3. Conclusions and Outlook.

3.1. Conclusions.

While the challenges to advancement and ultimately industrialisation and manufacture of organic photovoltaics are manifold, this work presents a study with a clear focus on the active layer processing, photophysics and morphology of all-polymer solar cells.

The impact of selenophene substitution on p-type donor copolymers and their effects on all-PSCs has been investigated. Two new donors bearing selenophene on the conjugated side chain (PBDB-S) and on the D-A backbone (PBDBS-T) were synthesised. Consequently, the systematic optimization of inverted solar cells of PBDB-T, PBDB-S and PBDBS-T donor copolymers with PNDIBS acceptor has been carried out. The three donors presented in this study all display complementary absorption with the narrow bandgap PNDIBS. Active layer processing revealed that inverted solar cells with a PCE of 9.14% with a J_{sc} of 18.38mA/cm^2, V_{oc} of 0.825V and FF of 0.607 could be realized through the film aging of PBDS-T:PNDIBS. In contrast, PBDB-S:PNDIBS displayed only a slight improvement in PCE over PBDB-T:PNDIBS with PCE of 8.38% as opposed to 8.08% respectively. Aside from the significant enhancement in zero-field mobility exhibited by both PBDB-S and PBDBS-T, multiple deviations in terms of recombination dynamics, exciton harvesting and morphology were observed. It is clear that the usage of selenophene on the conjugated side-chain has led to the formation of small and intermixed domains with little phase separation, while selenophene as a π-spacer has enabled the construction of crystalline and phase separated donor-acceptor pathways which allowed efficient exciton dissociation, balanced charge transport and suppressed bimolecular recombination.

As the application of the presented strategy is rather limited in the field of all-polymer solar cells, this work has helped advance the field of OPVs and revealed some important design considerations to be taken into account to synthesise state-of-the-art polymers. This work also shows the importance of device engineering and molecular design occurring concurrently to make a technological advancement. Through further investigation to advance the scope and overcome the limitations of the field, it is possible to usher the next generation of organic electronic devices.

3.2. Outlook.

Through recent efforts of several groups and researchers, all-PSCs have made steady progress in many aspects. As such, a focus towards driving this technology towards commercialisation is paramount. However, the task to increase the PCE of all-PSCs to 15%, which is often the metric used to gauge the marketability of OPVs, remains quite daunting. As demonstrated in the presented findings, PCEs up to 9.47% were obtained using high mobility donor and acceptor polymers with strong absorption coefficients concurrently. Thus, systems based on napthalenediimide biselenophene (PNDIBS) shows great promise in the all-PSC arena. However, there remain several problems to be addressed.

For instance, while it is true that PBDBS-T:PNDIBS based blends were found to have the greatest compatibility among the cases presented, it is worth noting that by narrowing the bandgap of donor polymer as a means to improve photocurrent, there is a compromise in the photoharvesting capability of the devices in the visible region. Also, the fill factors, which are critically dependent on morphology, are still relatively low. This photovoltaic parameter in particular is the most difficult to govern and least understood. Thus, the true potential of the said all-PSCs is not realized. It is possible to investigate alternate strategies such as the usage of ternary-

blend polymer solar cells to compensate for the lowered photoharvesting in the visible region by using polymers or small molecules with a strong absorbance in the blue region. However, such a strategy involves considerable complications, as it is difficult to determine the nature of interactions occurring in a bulk-heterojunction upon the introduction of a third phase *ab initio.* Alternatively, there have been recent studies reporting new families of p-type polymers based off napthodothiophene (NDT) as an alternative to benzodithiophene (BDT) with extended conjugation length and planarity with improved absorption in the 300-600 nm region.

Another major bottleneck to the industrialization of all-PSCs would be the reliance on halogenated solvents such as chloroform (CF), chlorobenzene (CB) and 1,2-dichlorobenzene (*o*-DCB). These can prove to be extremely hazardous. Although extremely challenging, realizing high-efficiency all-PSCs using environmental friendly or "green" solvents would have profound impacts on the field. Furthermore, improving solubility in solvents such as 2-methyl tetrahydrofuran (2-Me THF), tetrahydrofuran (THF) and toluene would also be desirable as it opens new prospects for greater control and tunability of morphology. It is possible to improve domain purity and control ordering of domains by using ideal solvents. Thus, rational selection of side-chains for polymers is also crucial. Some studies have already highlighted the potential of such a line research by fabricating all-PSCs that delivered among the highest PCEs (>10%) using sophisticated side-chain engineering in combination with active-layer processing with different solvents.

Lastly, scale-up of such systems could be another hurdle towards large-scale manufacture; as bench-top techniques such as spin-coating for interlayer and active layer deposition have the luxury of a smaller scale of operation, often times they result in film morphologies with remarkable

consistency free of defects. However, it is impractical to apply such a technique for substrates encompassing a larger area, as it may lead to morphological defects and inconsistencies in thickness. Furthermore, other variables such as thermal spalling, mechanical shear and stress and oxidation of organic layers come to the fore for larger flexible electronic devices. Therefore, further developments in alternate coating technologies such as roll-to-roll processing or blade coating would be beneficial to champion organic solar cells as a viable source of alternate energy.

References:

(1) Berger, P. R.; Kim, M.; Berger, P. R.; Kim, M. Polymer Solar Cells : P3HT : PCBM and Beyond. **2018**, *013508*.

(2) Zhang, Y.; Xu, Y.; Ford, M. J.; Li, F.; Sun, J.; Ling, X.; Wang, Y.; Gu, J.; Yuan, J.; Ma, W. Thermally Stable All-Polymer Solar Cells with High Tolerance on Blend Ratios. *Adv. Energy Mater.* **2018**, *8* (18), 1–10. https://doi.org/10.1002/aenm.201800029.

(3) Su, W.; Meng, Y.; Guo, X.; Fan, Q.; Zhang, M.; Jiang, Y.; Xu, Z.; Dai, Y.; Xie, B.; Liu, F.; Zhang, M.; Russell, T. P.; Li, Y. Efficient and Thermally Stable All-Polymer Solar Cells Based on a Fluorinated Wide-Bandgap Polymer Donor with High Crystallinity. *J. Mater. Chem. A* **2018**, *6* (34), 16403–16411. https://doi.org/10.1039/c8ta05376f.

(4) Ma, B. W.; Yang, C.; Gong, X.; Lee, K.; Heeger, A. J. Thermally Stable , Efficient Polymer Solar Cells with Nanoscale Control of the Interpenetrating Network Morphology **. **2005**, 1617–1622. https://doi.org/10.1002/adfm.200500211.

(5) Lin, Y.; Dong, S.; Li, Z.; Zheng, W.; Yang, J.; Liu, A.; Cai, W.; Liu, F.; Jiang, Y.; Russell, T. P.; Huang, F.; Wang, E.; Hou, L. Energy-Effectively Printed All-Polymer Solar Cells Exceeding 8.61% Efficiency. *Nano Energy* **2018**, *46* (February), 428–435. https://doi.org/10.1016/j.nanoen.2018.02.035.

(6) Galagan, Y.; de Vries, I. G.; Langen, A. P.; Andriessen, R.; Verhees, W. J. H.; Veenstra, S. C.; Kroon, J. M. Technology Development for Roll-to-Roll Production of Organic Photovoltaics. *Chem. Eng. Process. Process Intensif.* **2011**, *50* (5–6), 454–461. https://doi.org/10.1016/j.cep.2010.07.012.

(7) Krebs, F. C. Fabrication and Processing of Polymer Solar Cells: A Review of Printing and Coating Techniques. *Sol. Energy Mater. Sol. Cells* **2009**, *93* (4), 394–412. https://doi.org/10.1016/j.solmat.2008.10.004.

(8) Ge, N. An Overview on P3HT : PCBM , the Most Efficient Organic Solar Cell Material so Far . **2009**, No. Fig 1, 1–11.

(9) Balderrama, V. S.; Estrada, M.; Formentin, P.; Iñiguez, B.; Ferré-borrull, J.; Pallarés, J.; Nolasco, J. C.; Palomares, E. Performance and Degradation of Organic Solar Cells with Different P3HT : PCBM [70] Blend Composition. **2011**, 1–4. https://doi.org/10.1109/SCED.2011.5744224.

(10) Li, B. G.; Yao, Y.; Yang, H.; Shrotriya, V.; Yang, G.; Yang, Y. " Solvent Annealing " Effect in Polymer Solar Cells Based on Poly (3-Hexylthiophene) and Methanofullerenes **. **2007**, 1636–1644. https://doi.org/10.1002/adfm.200600624.

(11) Chen, D.; Nakahara, A.; Wei, D.; Nordlund, D.; Russell, T. P. P3HT/PCBM Bulk Heterojunction Organic Photovoltaics: Correlating Efficiency and Morphology. **2011**, 561–567.

(12) Yan, C.; Barlow, S.; Wang, Z.; Yan, H.; Jen, A. K. Y.; Marder, S. R.; Zhan, X. Non-Fullerene Acceptors for Organic Solar Cells. *Nat. Rev. Mater.* **2018**, *3*, 1–19. https://doi.org/10.1038/natrevmats.2018.3.

(13) Lu, L.; Zheng, T.; Wu, Q.; Schneider, A. M.; Zhao, D.; Yu, L. Recent Advances in Bulk Heterojunction Polymer Solar Cells. *Chem. Rev.* **2015**, *115* (23), 12666–12731. https://doi.org/10.1021/acs.chemrev.5b00098.

(14) Kang, H.; Lee, W.; Oh, J.; Kim, T.; Lee, C.; Kim, B. J. From Fullerene-Polymer to All-Polymer Solar Cells: The Importance of Molecular Packing, Orientation, and Morphology Control. *Acc. Chem. Res.* **2016**, *49* (11), 2424–2434. https://doi.org/10.1021/acs.accounts.6b00347.

(15) Zhou, N.; Facchetti, A. Naphthalenediimide (NDI) Polymers for All-Polymer Photovoltaics. *Mater. Today* **2018**, *21* (4), 377–390. https://doi.org/10.1016/j.mattod.2018.02.003.

(16) Wang, G.; Melkonyan, F. S.; Facchetti, A.; Marks, T. J. All-Polymer Solar Cells: Recent Progress, Challenges, and Prospects. *Angew. Chemie - Int. Ed.* **2019**, *58* (13), 4129–4142. https://doi.org/10.1002/anie.201808976.

(17) Ye, L.; Jiao, X.; Zhao, W.; Zhang, S.; Yao, H.; Li, S.; Ade, H.; Hou, J. Manipulation of Domain Purity and Orientational Ordering in High Performance All-Polymer Solar Cells. *Chem. Mater.* **2016**, *28* (17), 6178–6185. https://doi.org/10.1021/acs.chemmater.6b02222.

(18) Dang, M. T.; Hirsch, L.; Wantz, G. P3HT : PCBM , Best Seller in Polymer Photovoltaic Research. **2011**, 3597–3602. https://doi.org/10.1002/adma.201100792.

(19) Shockley, W.; Queisser, H. J. Detailed Balance Limit of Efficiency of P-n Junction Solar Cells. *J. Appl. Phys.* **1961**, *32* (3), 510–519. https://doi.org/10.1063/1.1736034.

(20) Vandewal, K.; Tvingstedt, K.; Gadisa, A.; Inganäs, O.; Manca, J. V. On the Origin of the Open-Circuit Voltage of Polymer-Fullerene Solar Cells. *Nat. Mater.* **2009**, *8* (11), 904–909. https://doi.org/10.1038/nmat2548.

(21) Yuan, J.; Zhang, Y.; Zhou, L.; Zhang, G.; Yip, H. L.; Lau, T. K.; Lu, X.; Zhu, C.; Peng,

H.; Johnson, P. A.; Leclerc, M.; Cao, Y.; Ulanski, J.; Li, Y.; Zou, Y. Single-Junction Organic Solar Cell with over 15% Efficiency Using Fused-Ring Acceptor with Electron-Deficient Core. *Joule* **2019**, *3* (4), 1140–1151. https://doi.org/10.1016/j.joule.2019.01.004.

(22) Halls, J. J. M.; Walsh, C. A.; Greenham, N. C.; Marseglia, E. A.; Friend, R. H.; Moratti, S. C.; Holmes, A. B. Efficient Photodiodes from Interpenetrating Polymer Networks. *Nature* **1995**, *376* (6540), 498–500. https://doi.org/10.1038/376498a0.

(23) Genene, Z.; Mammo, W.; Wang, E.; Andersson, M. R. Recent Advances in N-Type Polymers for All-Polymer Solar Cells. *Adv. Mater.* **2019**, *31* (22), 1–40. https://doi.org/10.1002/adma.201807275.

(24) Lee, C.; Lee, S.; Kim, G. U.; Lee, W.; Kim, B. J. Recent Advances, Design Guidelines, and Prospects of All-Polymer Solar Cells. *Chem. Rev.* **2019**, *119* (13), 8028–8086. https://doi.org/10.1021/acs.chemrev.9b00044.

(25) Hwang, Y. J.; Courtright, B. A. E.; Ferreira, A. S.; Tolbert, S. H.; Jenekhe, S. A. 7.7% Efficient All-Polymer Solar Cells. *Adv. Mater.* **2015**, *27* (31), 4578–4584. https://doi.org/10.1002/adma.201501604.

(26) Kim, T.; Kim, J. H.; Kang, T. E.; Lee, C.; Kang, H.; Shin, M.; Wang, C.; Ma, B.; Jeong, U.; Kim, T. S.; Kim, B. J. Flexible, Highly Efficient All-Polymer Solar Cells. *Nat. Commun.* **2015**, *6* (May), 1–7. https://doi.org/10.1038/ncomms9547.

(27) Wu, Y.; Schneider, S.; Walter, C.; Chowdhury, A. H.; Bahrami, B.; Wu, H. C.; Qiao, Q.; Toney, M. F.; Bao, Z. Fine-Tuning Semiconducting Polymer Self-Aggregation and Crystallinity Enables Optimal Morphology and High-Performance Printed All-Polymer

Solar Cells. *J. Am. Chem. Soc.* **2020**, *142* (1), 392–406. https://doi.org/10.1021/jacs.9b10935.

(28) Earmme, T.; Hwang, Y. J.; Subramaniyan, S.; Jenekhe, S. A. All-Polymer Bulk Heterojuction Solar Cells with 4.8% Efficiency Achieved by Solution Processing from a Co-Solvent. *Adv. Mater.* **2014**, *26* (35), 6080–6085. https://doi.org/10.1002/adma.201401490.

(29) Kolhe, N. B.; Tran, D. K.; Lee, H.; Kuzuhara, D.; Yoshimoto, N.; Koganezawa, T.; Jenekhe, S. A. New Random Copolymer Acceptors Enable Additive-Free Processing of 10.1% Efficient All-Polymer Solar Cells with Near-Unity Internal Quantum Efficiency. *ACS Energy Lett.* **2019**, *4*, 1162–1170. https://doi.org/10.1021/acsenergylett.9b00460.

(30) Lee, J. W.; Sung, M. J.; Kim, D.; Lee, S.; You, H.; Kim, F. S.; Kim, Y. H.; Kim, B. J.; Kwon, S. K. Naphthalene Diimide-Based Terpolymers with Controlled Crystalline Properties for Producing High Electron Mobility and Optimal Blend Morphology in All-Polymer Solar Cells. *Chem. Mater.* **2020**, *32* (6), 2572–2582. https://doi.org/10.1021/acs.chemmater.0c00055.

(31) Yao, H.; Bai, F.; Hu, H.; Arunagiri, L.; Zhang, J.; Chen, Y.; Yu, H.; Chen, S.; Liu, T.; Lai, J. Y. L.; Zou, Y.; Ade, H.; Yan, H. Efficient All-Polymer Solar Cells Based on a New Polymer Acceptor Achieving 10.3% Power Conversion Efficiency. *ACS Energy Lett.* **2019**, *4* (2), 417–422. https://doi.org/10.1021/acsenergylett.8b02114.

(32) Meng, Y.; Wu, J.; Guo, X.; Su, W.; Zhu, L.; Fang, J.; Zhang, Z.; Liu, F.; Zhang, M.; Russell, T. P.; Li, Y. 11 . 2 % Efficiency All-Polymer Solar Cells with High Open-Circuit.

2019.

(33) Wu, J.; Meng, Y.; Guo, X.; Zhu, L.; Liu, F.; Zhang, M. All-Polymer Solar Cells Based on a Novel Narrow-Bandgap Polymer Acceptor with Power Conversion Efficiency over 10%. *J. Mater. Chem. A* **2019**, *7* (27), 16190–16196. https://doi.org/10.1039/c9ta04611a.

(34) Zhu, L.; Zhong, W.; Qiu, C.; Lyu, B.; Zhou, Z.; Zhang, M.; Song, J.; Xu, J.; Wang, J.; Ali, J.; Feng, W.; Shi, Z.; Gu, X.; Ying, L.; Zhang, Y.; Liu, F. Aggregation-Induced Multilength Scaled Morphology Enabling 11.76% Efficiency in All-Polymer Solar Cells Using Printing Fabrication. *Adv. Mater.* **2019**, *31* (41), 1–8. https://doi.org/10.1002/adma.201902899.

(35) Jia, T.; Zhang, J.; Zhong, W.; Liang, Y.; Zhang, K.; Dong, S.; Ying, L.; Liu, F.; Wang, X.; Huang, F.; Cao, Y. 14.4% Efficiency All-Polymer Solar Cell With Broad Absorption and Low Energy Loss Enabled By a Novel Polymer Acceptor. *Nano Energy* **2020**, *72* (March), 104718. https://doi.org/10.1016/j.nanoen.2020.104718.

(36) Li, Z.; Ying, L.; Zhu, P.; Zhong, W.; Li, N.; Liu, F.; Huang, F.; Cao, Y. A Generic Green Solvent Concept Boosting the Power Conversion Efficiency of All-Polymer Solar Cells to 11%. *Energy Environ. Sci.* **2019**, *12* (1), 157–163. https://doi.org/10.1039/c8ee02863j.

(37) Kolhe, N. B.; Lee, H.; Kuzuhara, D.; Yoshimoto, N.; Koganezawa, T.; Jenekhe, S. A. All-Polymer Solar Cells with 9.4% Efficiency from Naphthalene Diimide-Biselenophene Copolymer Acceptor. *Chem. Mater.* **2018**, *30* (18), 6540–6548. https://doi.org/10.1021/acs.chemmater.8b03229.

(38) Tran, D. K.; Kolhe, N. B.; Hwang, Y. J.; Kuzuhara, D.; Koganezawa, T.; Jenekhe, S. A.

Effects of a Fluorinated Donor Polymer on the Morphology, Photophysics, and Performance of All-Polymer Solar Cells Based on Naphthalene Diimide-Arylene Copolymer Acceptors. *ACS Appl. Mater. Interfaces* **2020**, *12* (14), 16490–16502. https://doi.org/10.1021/acsami.0c01382.

(39) Hwang, Y. J.; Murari, N. M.; Jenekhe, S. A. New N-Type Polymer Semiconductors Based on Naphthalene Diimide and Selenophene Derivatives for Organic Field-Effect Transistors. *Polym. Chem.* **2013**, *4* (11), 3187–3195. https://doi.org/10.1039/c3py00325f.

(40) Jenekhe, S. A.; Yi, S. Efficient Photovoltaic Cells from Semiconducting Polymer Heterojunctions. *Appl. Phys. Lett.* **2000**, *77* (17), 2635–2637. https://doi.org/10.1063/1.1320022.

(41) Fan, B.; Zhong, W.; Ying, L.; Zhang, D.; Li, M.; Lin, Y.; Xia, R.; Liu, F.; Yip, H. L.; Li, N.; Ma, Y.; Brabec, C. J.; Huang, F.; Cao, Y. Surpassing the 10% Efficiency Milestone for 1-Cm2 All-Polymer Solar Cells. *Nat. Commun.* **2019**, *10* (1). https://doi.org/10.1038/s41467-019-12132-6.

(42) Li, Z.; Xu, X.; Zhang, W.; Meng, X.; Ma, W.; Yartsev, A.; Inganäs, O.; Andersson, M. R.; Janssen, R. A. J.; Wang, E. High Performance All-Polymer Solar Cells by Synergistic Effects of Fine-Tuned Crystallinity and Solvent Annealing. *J. Am. Chem. Soc.* **2016**, *138* (34), 10935–10944. https://doi.org/10.1021/jacs.6b04822.

(43) Hwang, Y. J.; Earmme, T.; Courtright, B. A. E.; Eberle, F. N.; Jenekhe, S. A. N-Type Semiconducting Naphthalene Diimide-Perylene Diimide Copolymers: Controlling Crystallinity, Blend Morphology, and Compatibility Toward High-Performance All-

Polymer Solar Cells. *J. Am. Chem. Soc.* **2015**, *137* (13), 4424–4434. https://doi.org/10.1021/ja513260w.

(44) Wang, G.; Eastham, N. D.; Aldrich, T. J.; Ma, B.; Manley, E. F.; Chen, Z.; Chen, L. X.; de la Cruz, M. O.; Chang, R. P. H.; Melkonyan, F. S.; Facchetti, A.; Marks, T. J. Photoactive Blend Morphology Engineering through Systematically Tuning Aggregation in All-Polymer Solar Cells. *Adv. Energy Mater.* **2018**, *8* (12), 1–13. https://doi.org/10.1002/aenm.201702173.

(45) Liu, Q.; Jiang, Y.; Jin, K.; Qin, J.; Xu, J.; Li, W.; Xiong, J.; Liu, J.; Xiao, Z.; Sun, K.; Yang, S.; Zhang, X.; Ding, L. 18% Efficiency Organic Solar Cells. *Sci. Bull.* **2020**, *65* (4), 272–275. https://doi.org/10.1016/j.scib.2020.01.001.

(46) Feng, K.; Yuan, J.; Bi, Z.; Ma, W.; Xu, X.; Zhang, G.; Peng, Q. Low-Energy-Loss Polymer Solar Cells with 14.52% Efficiency Enabled by Wide-Band-Gap Copolymers. *iScience* **2019**, *12*, 1–12. https://doi.org/10.1016/j.isci.2018.12.027.

(47) Zhang, S.; Qin, Y.; Zhu, J.; Hou, J. Over 14% Efficiency in Polymer Solar Cells Enabled by a Chlorinated Polymer Donor. *Adv. Mater.* **2018**, *30* (20), 1–7. https://doi.org/10.1002/adma.201800868.

(48) Xu, X.; Li, Z.; Bi, Z.; Yu, T.; Ma, W.; Feng, K.; Li, Y.; Peng, Q. Highly Efficient Nonfullerene Polymer Solar Cells Enabled by a Copper(I) Coordination Strategy Employing a 1,3,4-Oxadiazole-Containing Wide-Bandgap Copolymer Donor. *Adv. Mater.* **2018**, *30* (28), 1–8. https://doi.org/10.1002/adma.201800737.

(49) Xu, X.; Yu, T.; Bi, Z.; Ma, W.; Li, Y.; Peng, Q. Realizing Over 13% Efficiency in Green-

Solvent-Processed Nonfullerene Organic Solar Cells Enabled by 1,3,4-Thiadiazole-Based Wide-Bandgap Copolymers. *Adv. Mater.* **2018**, *30* (3), 1–8. https://doi.org/10.1002/adma.201703973.

(50) Chao, P.; Guo, M.; Zhu, Y.; Chen, H.; Pu, M.; Huang, H.-H.; Meng, H.; Yang, C.; He, F. Enhanced Photovoltaic Performance by Synergistic Effect of Chlorination and Selenophene π-Bridge. *Macromolecules* **2020**. https://doi.org/10.1021/acs.macromol.0c00405.

(51) Zhong, X.; Chen, H.; Wang, M.; Gan, S.; He, Q.; Chen, W.; He, F. Synergistic Effect of Chlorination and Selenophene: Achieving Elevated Solar Conversion in Highly Aggregated Systems. *Macromolecules* **2019**, *52* (6), 2393–2401. https://doi.org/10.1021/acs.macromol.8b02445.

(52) Cao, F. Y.; Tseng, C. C.; Lin, F. Y.; Chen, Y.; Yan, H.; Cheng, Y. J. Selenophene-Incorporated Quaterchalcogenophene-Based Donor-Acceptor Copolymers to Achieve Efficient Solar Cells with Jsc Exceeding 20 MA/Cm2. *Chem. Mater.* **2017**, *29* (23), 10045–10052. https://doi.org/10.1021/acs.chemmater.7b03688.

(53) Wang, H. C.; Li, Q. Y.; Yin, H. B.; Ren, X.; Yao, K.; Zheng, Y.; Xu, Y. X. Synergistic Effects of Selenophene and Extended Ladder-Type Donor Units for Efficient Polymer Solar Cells. *Macromol. Rapid Commun.* **2018**, *39* (2), 1–6. https://doi.org/10.1002/marc.201700483.

(54) Xu, Z.; Fan, Q.; Meng, X.; Guo, X.; Su, W.; Ma, W.; Zhang, M.; Li, Y. Selenium-Containing Medium Bandgap Copolymer for Bulk Heterojunction Polymer Solar Cells

with High Efficiency of 9.8%. *Chem. Mater.* **2017**, *29* (11), 4811–4818. https://doi.org/10.1021/acs.chemmater.7b00729.

(55) Liao, X.; Shi, X.; Zhang, M.; Gao, K.; Zuo, L.; Liu, F.; Chen, Y.; Jen, A. K. Y. Fused Selenophene-Thieno[3,2-B] Thiophene-Selenophene (ST)-Based Narrow-Bandgap Electron Acceptor for Efficient Organic Solar Cells with Small Voltage Loss. *Chem. Commun.* **2019**, *55* (57), 8258–8261. https://doi.org/10.1039/c9cc03585k.

(56) Liang, Z.; Li, M.; Zhang, X.; Wang, Q.; Jiang, Y.; Tian, H.; Geng, Y. Near-Infrared Absorbing Non-Fullerene Acceptors with Selenophene as π Bridges for Efficient Organic Solar Cells. *J. Mater. Chem. A* **2018**, *6* (17), 8059–8067. https://doi.org/10.1039/c8ta00783g.

(57) Li, C.; Xia, T.; Song, J.; Fu, H.; Ryu, H. S.; Weng, K.; Ye, L.; Woo, H. Y.; Sun, Y. Asymmetric Selenophene-Based Non-Fullerene Acceptors for High-Performance Organic Solar Cells. *J. Mater. Chem. A* **2019**, *7* (4), 1435–1441. https://doi.org/10.1039/c8ta11197a.

(58) Zhong, L.; Bin, H.; Angunawela, I.; Jia, Z.; Qiu, B.; Sun, C.; Li, X.; Zhang, Z.; Ade, H.; Li, Y. Effect of Replacing Thiophene by Selenophene on the Photovoltaic Performance of Wide Bandgap Copolymer Donors. *Macromolecules* **2019**, *52* (12), 4776–4784. https://doi.org/10.1021/acs.macromol.9b00484.

(59) Gao, X.; Li, Y.; Yu, L.; Hou, F.; Zhu, T.; Bao, X.; Li, F.; Sun, M.; Yang, R. The Regulation of π-Bridge of Indacenodithiophene-Based Donor-π-Acceptor Conjugated Polymers toward Efficient Polymer Solar Cells. *Dye. Pigment.* **2019**, *162* (October 2018),

43–51. https://doi.org/10.1016/j.dyepig.2018.10.008.

(60) Earmme, T.; Hwang, Y. J.; Murari, N. M.; Subramaniyan, S.; Jenekhe, S. A. All-Polymer Solar Cells with 3.3% Efficiency Based on Naphthalene Diimide-Selenophene Copolymer Acceptor. *J. Am. Chem. Soc.* **2013**, *135* (40), 14960–14963. https://doi.org/10.1021/ja4085429.

(61) Li, Y.; Li, Z.; Peng, Q.; Yu, T.; Zhang, G.; Xu, X. Highly Efficient Non-Fullerene Polymer Solar Cells Enabled by Wide Bandgap Copolymers With Conjugated Selenyl Side Chains. *Sol. RRL* **2018**, *2* (10), 1800186. https://doi.org/10.1002/solr.201800186.

(62) Lee, C.; Lee, S.; Kim, G. U.; Lee, W.; Kim, B. J. Recent Advances, Design Guidelines, and Prospects of All-Polymer Solar Cells. *Chemical Reviews*. American Chemical Society July 10, 2019, pp 8028–8086. https://doi.org/10.1021/acs.chemrev.9b00044.

(63) Kuzuhara, D.; Yoshimoto, N.; Lee, H.; Koganezawa, T.; Kolhe, N. B.; Jenekhe, S. A. All-Polymer Solar Cells with 9.4% Efficiency from Naphthalene Diimide-Biselenophene Copolymer Acceptor. *Chem. Mater.* **2018**, *30* (18), 6540–6548. https://doi.org/10.1021/acs.chemmater.8b03229.

(64) Qian, D.; Ye, L.; Zhang, M.; Liang, Y.; Li, L.; Huang, Y.; Guo, X.; Zhang, S.; Tan, Z.; Hou, J. Design, Application, and Morphology Study of a New Photovoltaic Polymer with Strong Aggregation in Solution State. *Macromolecules* **2012**, *45* (24), 9611–9617. https://doi.org/10.1021/ma301900h.

(65) Zhong, L.; Bin, H.; Angunawela, I.; Jia, Z.; Qiu, B.; Sun, C.; Li, X.; Zhang, Z.; Ade, H.; Li, Y. Effect of Replacing Thiophene by Selenophene on the Photovoltaic Performance of

Wide Bandgap Copolymer Donors. *Macromolecules* **2019**, *52* (12), 4776–4784. https://doi.org/10.1021/acs.macromol.9b00484.

(66) Ashraf, R. S.; Meager, I.; Nikolka, M.; Kirkus, M.; Planells, M.; Schroeder, B. C.; Holliday, S.; Hurhangee, M.; Nielsen, C. B.; Sirringhaus, H.; McCulloch, I. Chalcogenophene Comonomer Comparison in Small Band Gap Diketopyrrolopyrrole-Based Conjugated Polymers for High-Performing Field-Effect Transistors and Organic Solar Cells. *J. Am. Chem. Soc.* **2015**, *137* (3), 1314–1321. https://doi.org/10.1021/ja511984q.

(67) Heumueller, T.; Burke, T. M.; Mateker, W. R.; Sachs-Quintana, I. T.; Vandewal, K.; Brabec, C. J.; McGehee, M. D. Disorder-Induced Open-Circuit Voltage Losses in Organic Solar Cells during Photoinduced Burn-In. *Adv. Energy Mater.* **2015**, *5* (14), 1–8. https://doi.org/10.1002/aenm.201500111.

(68) Heumueller, T.; Mateker, W. R.; Sachs-Quintana, I. T.; Vandewal, K.; Bartelt, J. A.; Burke, T. M.; Ameri, T.; Brabec, C. J.; McGehee, M. D. Reducing Burn-in Voltage Loss in Polymer Solar Cells by Increasing the Polymer Crystallinity. *Energy Environ. Sci.* **2014**, *7* (9), 2974–2980. https://doi.org/10.1039/c4ee01842g.

(69) Sulas, D. B.; Yao, K.; Intemann, J. J.; Williams, S. T.; Li, C. Z.; Chueh, C. C.; Richards, J. J.; Xi, Y.; Pozzo, L. D.; Schlenker, C. W.; Jen, A. K. Y.; Ginger, D. S. Open-Circuit Voltage Losses in Selenium-Substituted Organic Photovoltaic Devices from Increased Density of Charge-Transfer States. *Chem. Mater.* **2015**, *27* (19), 6583–6591. https://doi.org/10.1021/acs.chemmater.5b02133.

(70) Park, M. S.; Kim, F. S. Synergistic Effects of Processing Additives and Thermal Annealing on Nanomorphology and Hole Mobility of Poly(3-Hexylthiophene) Thin Films. *Polymers (Basel).* **2019**, *11* (1), 1–11. https://doi.org/10.3390/polym11010112.

(71) Liu, X.; Wang, H. Q.; Li, Y.; Gui, Z.; Ming, S.; Usman, K.; Zhang, W.; Fang, J. Regular Organic Solar Cells with Efficiency over 10% and Promoted Stability by Ligand- and Thermal Annealing-Free Al-Doped ZnO Cathode Interlayer. *Adv. Sci.* **2017**, *4* (8), 1–8. https://doi.org/10.1002/advs.201700053.

(72) Lin, Z.; Chang, J.; Zhang, C.; Zhang, J.; Wu, J.; Hao, Y. Low Temperature Aqueous Solution-Processed Li Doped ZnO Buffer Layers for High Performance Inverted Organic Solar Cells. *J. Mater. Chem. C* **2016**, *4* (25), 6169–6175. https://doi.org/10.1039/c6tc00760k.

(73) Soultati, A.; Fakharuddin, A.; Polydorou, E.; Drivas, C.; Kaltzoglou, A.; Haider, M. I.; Kournoutas, F.; Fakis, M.; Palilis, L. C.; Kennou, S.; Davazoglou, D.; Falaras, P.; Argitis, P.; Gardelis, S.; Kordatos, A.; Chroneos, A.; Schmidt-Mende, L.; Vasilopoulou, M. Lithium Doping of ZnO for High Efficiency and Stability Fullerene and Non-Fullerene Organic Solar Cells. *ACS Appl. Energy Mater.* **2019**, *2* (3), 1663–1675. https://doi.org/10.1021/acsaem.8b01658.

(74) Zhang, S.; Ye, L.; Zhao, W.; Liu, D.; Yao, H.; Hou, J. Side Chain Selection for Designing Highly Efficient Photovoltaic Polymers with 2D-Conjugated Structure. *Macromolecules* **2014**, *47* (14), 4653–4659. https://doi.org/10.1021/ma500829r.

(75) Gao, W.; An, Q.; Ming, R.; Xie, D.; Wu, K.; Luo, Z.; Zou, Y.; Zhang, F.; Yang, C. Side

Group Engineering of Small Molecular Acceptors for High-Performance Fullerene-Free Polymer Solar Cells: Thiophene Being Superior to Selenophene. *Adv. Funct. Mater.* **2017**, *27* (34), 1–10. https://doi.org/10.1002/adfm.201702194.

(76) Saadeh, H. A.; Lu, L.; He, F.; Bullock, J. E.; Wang, W.; Carsten, B.; Yu, L. Polyselenopheno[3,4-b]Selenophene for Highly Efficient Bulk Heterojunction Solar Cells. *ACS Macro Lett.* **2012**, *1* (3), 361–365. https://doi.org/10.1021/mz300004t.

(77) Patra, A.; Bendikov, M. Polyselenophenes. *J. Mater. Chem.* **2010**, *20* (3), 422–433. https://doi.org/10.1039/b908983g.

(78) Fan, B.; Ying, L.; Zhu, P.; Pan, F.; Liu, F.; Chen, J.; Huang, F.; Cao, Y. All-Polymer Solar Cells Based on a Conjugated Polymer Containing Siloxane-Functionalized Side Chains with Efficiency over 10%. *Adv. Mater.* **2017**, *29* (47), 1–7. https://doi.org/10.1002/adma.201703906.

APPENDIX

TABLE OF CONTENTS

SUPPORTING FIGURES

SUPPORTING TABLES

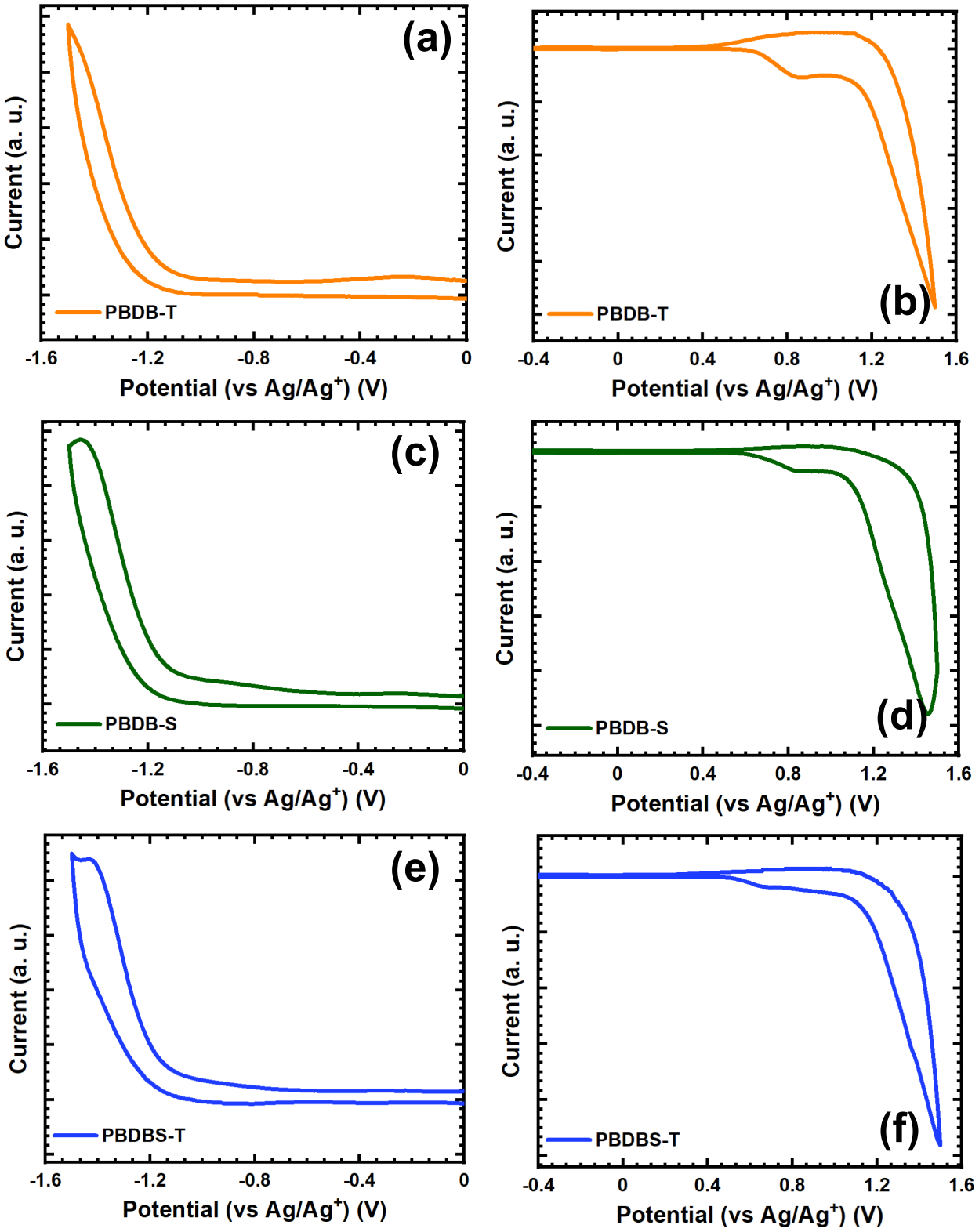

Figure S1. Cyclic voltammograms of PBDB-T (a, b), PBDB-S (c, d) and PBDBS-T (e, f) in 0.1 M $BuNPF_6$ solution in acetonitrile at a scan rate of 50 mV/s.

Table S3. Summary of onset potentials of PBDB-T, PBDB-S and PBDBS-T donor copolymer thin-films respectively.

Donor copolymer:	Reduction onset potential ($E_{red\text{-}onset}$) (V)	Oxidation onset potential ($E_{ox\text{-}onset}$) (V)
PBDB-T	0.65	-1.20
PBDB-S	0.65	-1.18
PBDBS-T	0.52	-1.18

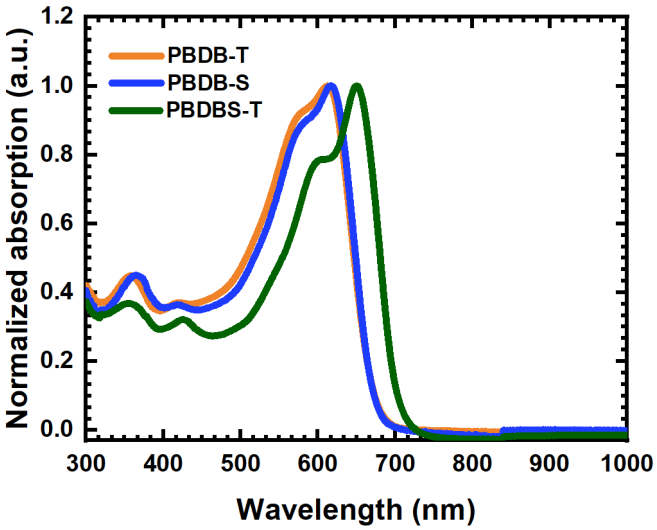

Figure S2. UV-Vis absorption spectra of dilute solutions (<10^{-6} M) of PBDB-T, PBDB-S and PBDBS-T donor copolymers. PBDB-T and PBDB-S were dissolved in chlorobenzene solvent, while PBDBS-T in 1,2-dichlorobenzene.

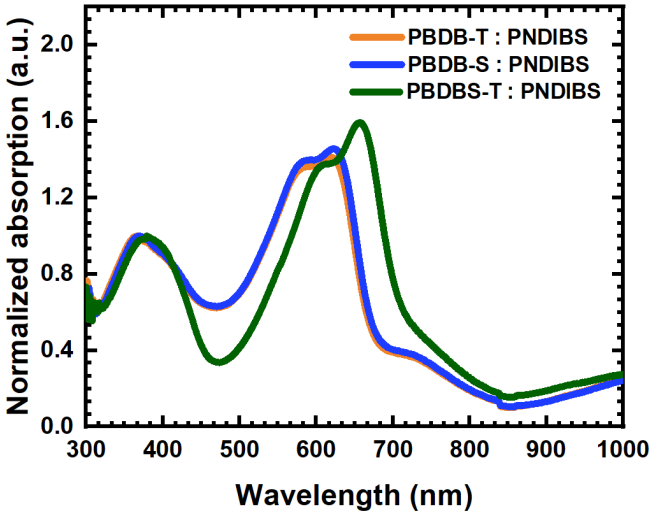

Figure S3. UV-Vis absorption spectra of thin-films of PBDB-T:PNDIBS (1:0.4 wt/wt), PBDB-S:PNDIBS (1:0.4 wt/wt) and PBDBS-T:PNDIBS (1:0.6 wt/wt) blends. PBDB-T:PNDIBS and PBDB-S:PNDIBS were dissolved in chlorobenzene solvent, while PBDBS-T:PNDIBS in 1,2-dichlorobenzene.

Table S4. Effect of blend composition on the performance of PBDBS-T:PNDIBS All-PSCs. Devices subjected to thermal annealing at 130 °C.

D:A ratio (wt/wt)	J_{sc} (mA/cm^2)	V_{oc} (V)	FF	PCE_{ave} (%)
1:0.4	12.859 (±0.25)	0.79 (±0.01)	0.547 (±0.018)	5.494 (±0.133)
1:0.6	13.847 (±1.066)	0.8 (±0.01)	0.540 (±0.042)	5.981 (±0.481)
1:0.8	10.1665 (±0.641)	0.79 (±0)	0.596 (±0.025)	4.784 (±0.389)
1:1	7.099 (±1.121)	0.79 (±0.01)	0.596 (±0.011)	3.302 (±0.457)

The average PCE values were generated using 4 separate devices. Active layers with thicknesses of c.a. 55 nm were obtained.

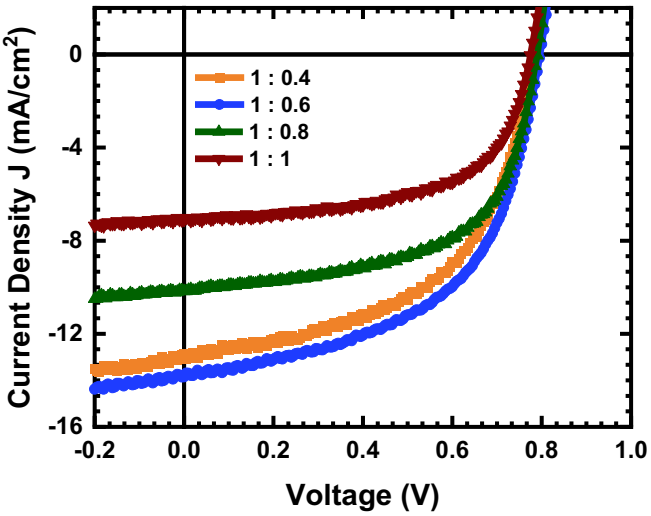

Figure S4. Current density (*J*) - Voltage (*V*) characteristics of PBDBS-T:PNDIBS for different blend compositions (wt/wt). All devices subjected to thermal annealing at 130 °C

Table S5. Effect of different annealing temperatures on the performance of PBDBS-T:PNDIBS (1:0.6 wt/wt) All-PSCs.

Annealing temperature	J_{sc} (mA/cm^2)	V_{oc} (V)	FF	PCE$_{ave}$ (%)
110 °C	14.297 (±0.867)	0.795 (±0.005)	0.552 (±0.011)	6.234 (±0.199)
130 °C	15.134 (±1.266)	0.785 (±0.01)	0.546 (±0.037)	6.531 (±0.484)
150 °C	16.373 (±1.542)	0.78 (±0)	0.538 (±0.016)	7.226 (±0.511)
175 °C	13.414 (±0.676)	0.78 (±0.005)	0.509 (±0.046)	5.396 (±0.346)

The average PCE values were generated using 4 separate devices. Active layers with thicknesses of c.a. 75 nm were obtained.

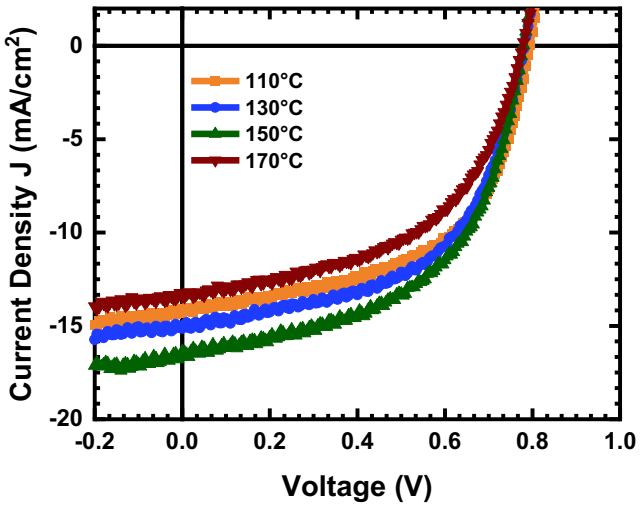

Figure S5. Current density (*J*) - Voltage (*V*) characteristics of PBDBS-T:PNDIBS (1:0.6 wt/wt) at different annealing temperatures.

Table S6. Exploring different processing additive and their impact on the performance of PBDBS-T:PNDIBS (1:0.6 wt/wt) devices annealed at 150 °C.

Additive used: (0.5% v/v)	J_{sc} (mA/cm^2)	V_{oc} (V)	FF	PCE (%)
No additive	17.1 (±0.42)	0.785 (±0.005)	0.571 (±0.011)	7.67 (±0.29)
DPE	12.51 (±0.18)	0.76 (±0.01)	0.508 (±0)	4.83 (±0.1)
DIO	13.98 (±0.3)	0.77 (±0)	0.50 (±0.016)	5.375 (±0.48)
ODT	14.42 (±0.76)	0.755 (±0.005)	0.47 (±0.04)	5.11 (±0.346)
CN	16.37 (±0.25)	0.78 (±0.005)	0.524 (±0.005)	6.946 (±0.01)
1,2,4-TCB	16.513 (±0.18)	0.8 (±0.01)	0.582 (±0)	7.688 (±0.1)

The average PCE values were generated using 4 separate devices. Active layers with thicknesses of c.a. 100 nm were obtained.

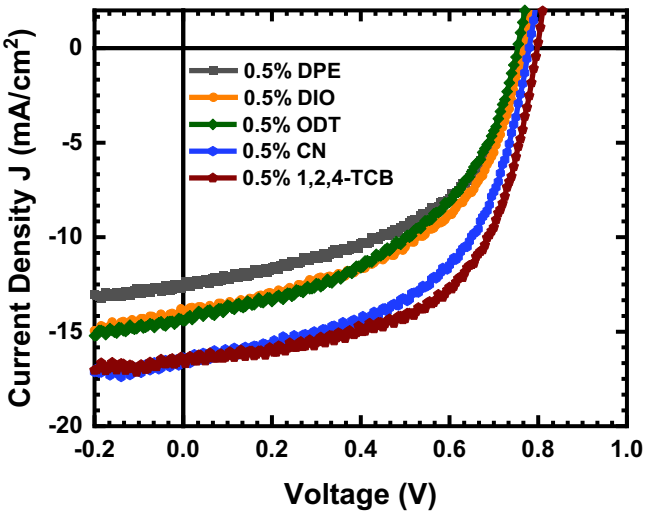

Figure S6. Current density (*J*) - Voltage (*V*) characteristics of PBDBS-T:PNDIBS (1:0.6 wt/wt) devices with different processing additives (0.5% v/v) annealed at 150 °C.

Table S7. Effect of variation of 1,2,4-Trichlorobenzene concentration on the performance of PBDBS-T:PNDIBS (1:0.6 wt/wt) devices annealed at 150 °C.

Additive conc: (vol%)	J_{sc} (mA/cm^2)	V_{oc} (V)	FF	PCE (%)
Blank	17.1 (±0.42)	0.785 (±0.005)	0.571 (±0.011)	7.67 (±0.29)
0.5%	16.513 (±0.18)	0.8 (±0.01)	0.582 (±0)	7.688 (±0.1)
1%	17.136 (±0.3)	0.805 (±0)	0.565 (±0.016)	7.789 (±0.48)
2%	17.354 (±0.76)	0.8 (±0.005)	0.602 (±0.04)	8.24 (±0.346)
3%	17.666 (±0.25)	0.79 (±0.005)	0.568 (±0.005)	7.771 (±0.01)
4%	17.52 (±0.25)	0.775 (±0.005)	0.51 (±0.005)	6.919 (±0.01)

The average PCE values were generated using 4 separate devices. Active layers with thicknesses of c.a. 100 nm were obtained.

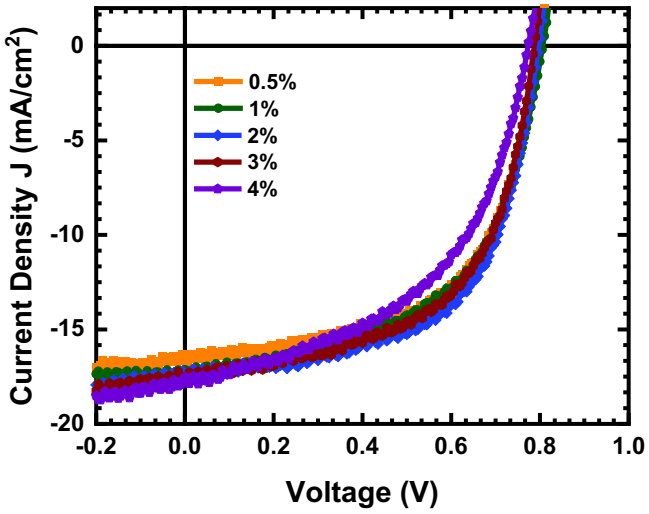

Figure S7. Current density (*J*) - Voltage (*V*) characteristics of PBDBS-T:PNDIBS (1:0.6 wt/wt) devices at different additive (1,2,4-Trichlorobenzene) concentrations annealed at 150 °C.

Table S8. Effect of different pre-treatment pathways on the photovoltaic performance of PBDBS-T:PNDIBS (1:0.6 wt/wt)

Pre-treatment:	J_{sc} (mA/cm^2)	V_{oc} (V)	FF	PCE_{ave} (%)
Annealed	17.1 (±0.42)	0.785 (±0.005)	0.571 (±0.011)	7.67 (±0.29)
Annealed + 2% TCB	17.354 (±0.76)	0.8 (±0.005)	0.602 (±0.04)	8.24 (±0.346)
Aged (3hrs)	17.62 (±0.66)	0.815 (±0.005)	0.582 (±0.01)	8.44 (±0.30)
Aged (3hrs) + 2% TCB	18.38 (±1.066)	0.825 (±0.01)	0.607 (±0.021)	9.15 (±0.184)

The average PCE values were generated using 8 separate devices. Active layers with thicknesses of c.a. 100nm were obtained.

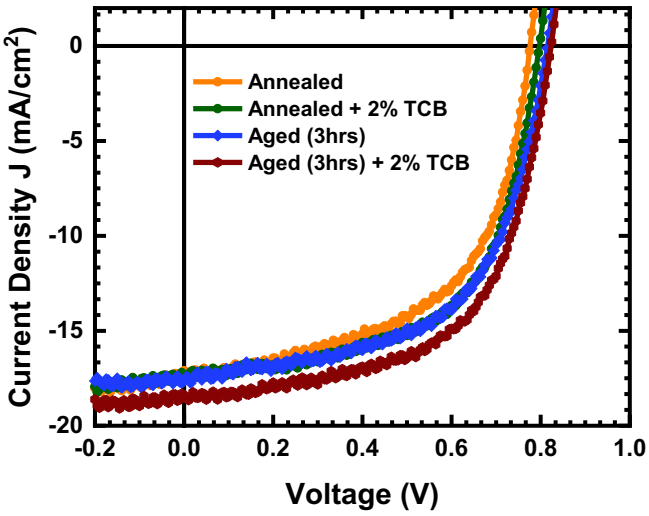

Figure S8. Current density (*J*) - Voltage (*V*) characteristics of PBDBS-T:PNDIBS (1:0.6 wt/wt) devices subjected to different pre-treatment pathways.

Table S9. Effect of different pre-treatment pathways on the photovoltaic performance of PBDB-T:PNDIBS (1:0.4 wt/wt)

Pre-treatment:	J_{sc} (mA/cm^2)	V_{oc} (V)	FF	PCE_{ave} (%)
Aged (3hrs)	14.32	0.870	0.522	6.47 (±0.32)
Annealed (130 °C)	15.11	0.865	0.581	7.45 (±0.24)
Annealed + 0.5% DPE	15.76	0.855	0.600	8.08 (±0.1)

The average PCE values were generated using 8 separate devices. Active layers with thicknesses of c.a. 100nm were obtained.

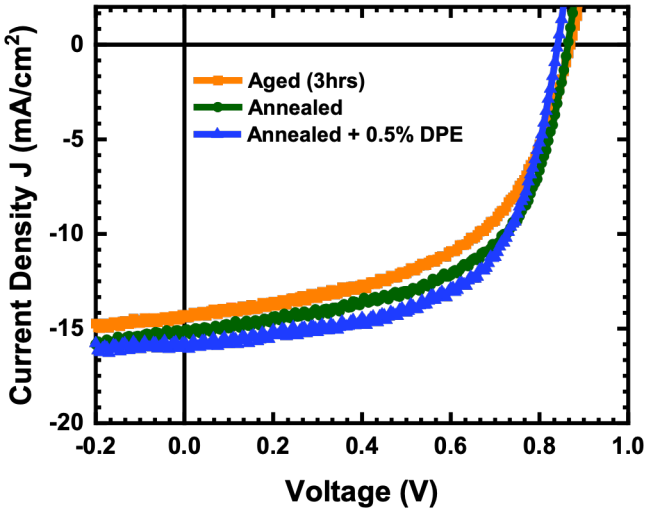

Figure S9. Current density (*J*) - Voltage (*V*) characteristics of PBDB-T:PNDIBS (1:0.4 wt/wt) devices subjected to different pre-treatment pathways.

Table S10. Effect of different pre-treatment pathways on the photovoltaic performance of PBDB-S:PNDIBS (1:0.4 wt/wt)

Pre-treatment:	J_{sc} (mA/cm^2)	V_{oc} (V)	FF	PCE_{ave} (%)
Aged (3hrs)	15.01	0.865	0.517	6.71 (±0.18)
Annealed (175 °C)	16.77	0.845	0.549	7.69 (±0.19)
Annealed (175 °C)	17.51	0.845	0.563	8.38 (±0.23)

The average PCE values were generated using 8 separate devices. Active layers with thicknesses of c.a. 100nm were obtained.

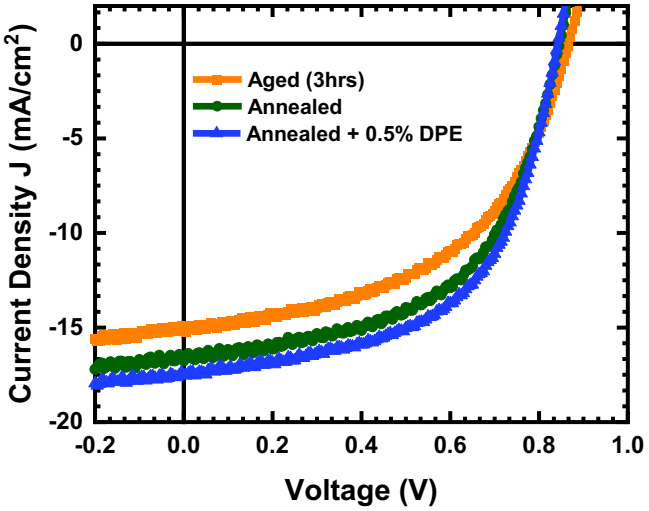

Figure S10. Current density (*J*) - Voltage (*V*) characteristics of PBDB-S:PNDIBS (1:0.4 wt/wt) devices subjected to different pre-treatment pathways.

Table S11. Employing a conventional device architecture with ITO/PEDOT:PSS/Active layer/PFN-Br/Al.

Active layer composition:	J_{sc} (mA/cm^2)	V_{oc} (V)	FF	PCE_{ave} (%)
PBDB-T : PNDIBS	16.52 (±0.32)	0.850 (±0.005)	0.614 (±0.007)	8.38 (±0.21)
PBDB-S : PNDIBS	17.78 (±0.15)	0.850 (±0.005)	0.592 (±0.005)	8.82 (±0.16)
PBDBS-T : PNDIBS	18.26 (±0.77)	0.825 (±0.01)	0.635 (±0.01)	9.47 (±0.29)

The average PCE values were generated using 8 separate devices. Active layers with thicknesses of c.a. 100nm were obtained.

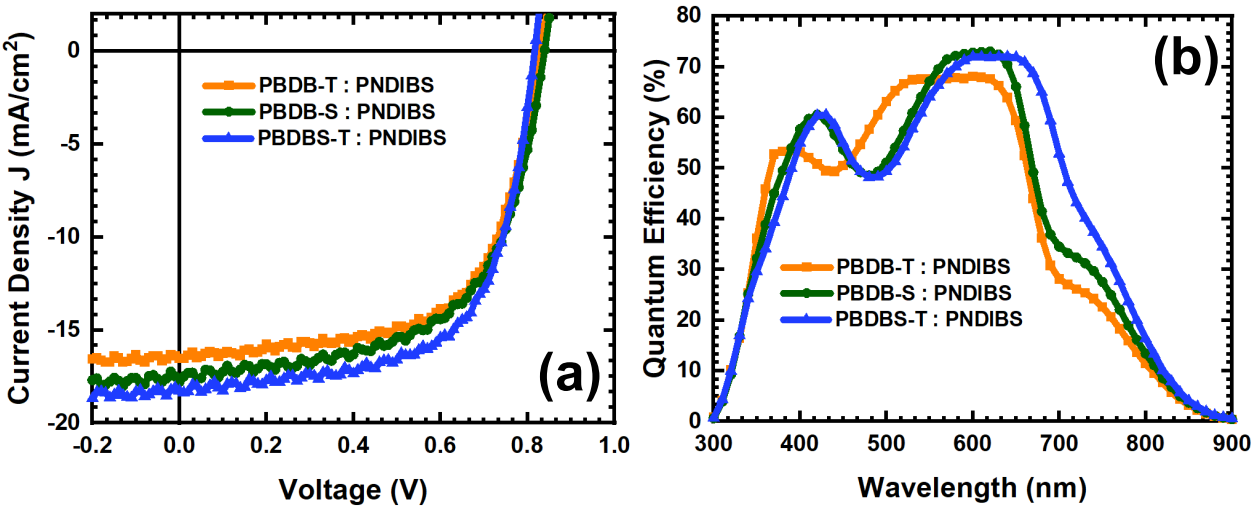

Figure S11. Current density (*J*) - Voltage (*V*) characteristics under AM 1.5G illumination (a) and External quantum efficiency (EQE) spectra (b) for optimized blends of PBDB-T:PNDIBS, PBDB-S:PNDIBS and PBDBS-T:PNDIBS based Conventional All-Polymer Solar Cells. The architecture ITO/PEDOT:PSS/Active layer/PFN-Br/Al was used.

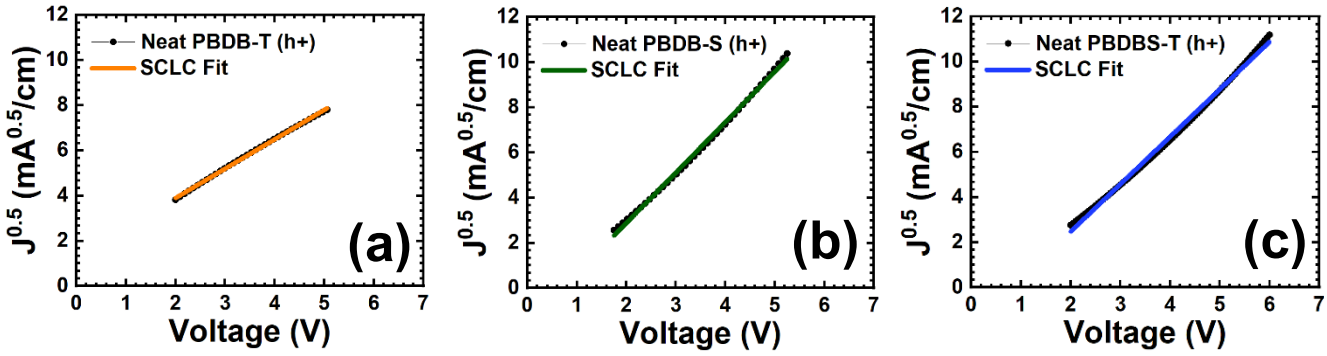

Figure S12. *J-V* curves of hole-only devices measured by Space-Charge Limited Current (SCLC) method for neat films of (a) PBDB-T, (b) PBDB-S and (c) PBDBS-T. All neat active layers had a thickness of c.a. 350 nm.

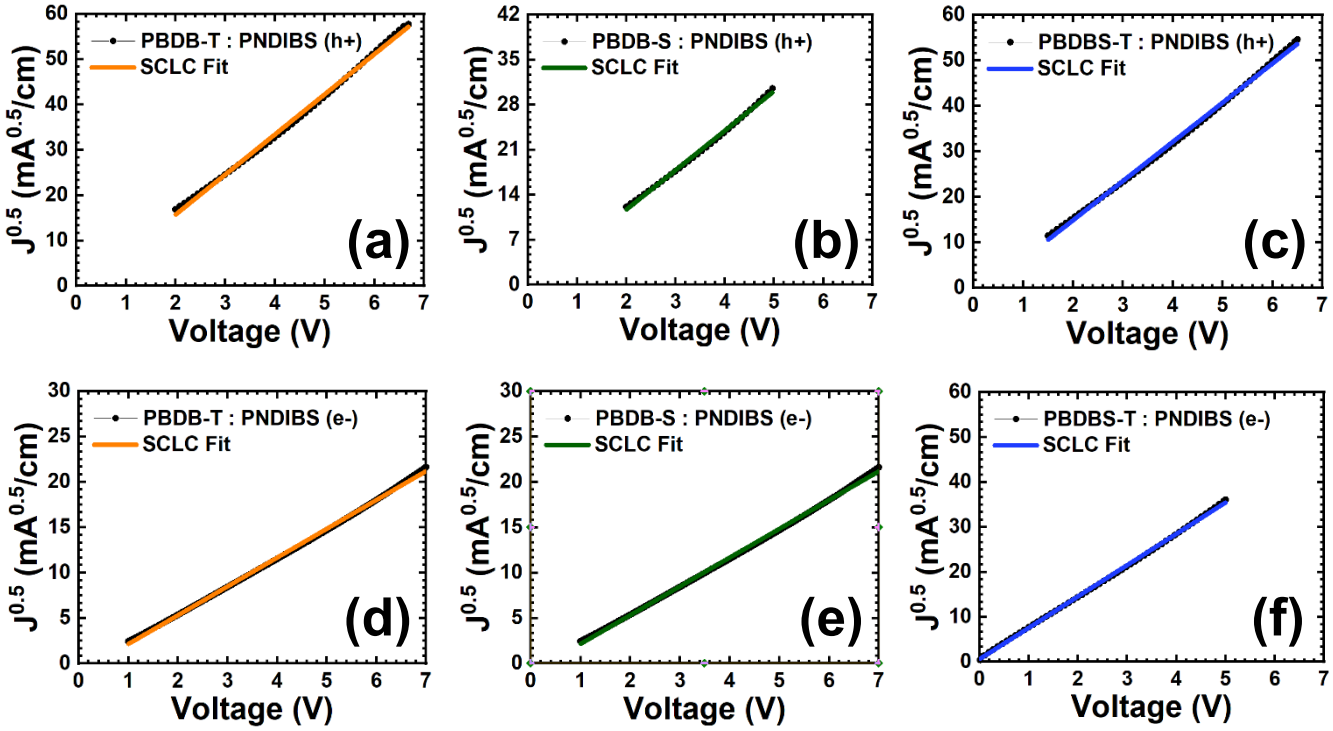

Figure S13. *J-V* curves of hole-only devices (a, b, c) and electron-only devices (d, e, f) measured Space-Chage Limited Current (SCLC) method for optimized PBDB-T:PNDIBS, PBDB-S:PNDIBS and PBDBS-T:PNDIBS blends. All optimized active layers had a thickness of c.a. 150 nm.

Table S12. Summary of exciton dissociation parameters and their correlation to J_{sc} and FF for optimized inverted All-PSCs.

System	J_{sc} (mA/cm^2)	J_{sat} (mA/cm^2)	$P(E, T) = J_{sc}/J_{sat}$	Fill Factor FF
PBDB-T:PNDIBS	15.76	16.69	0.945	0.603
PBDB-S:PNDIBS	17.51	18.68	0.94	0.563
PBDBS-T:PNDIBS	18.38	19.17	0.952	0.607

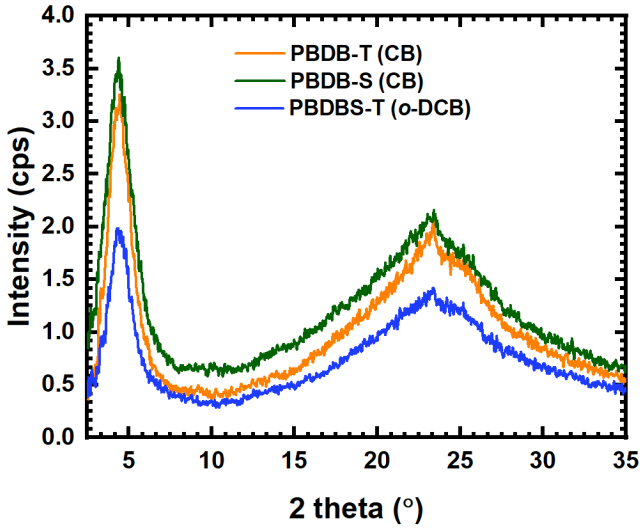

Figure S14. X-Ray Diffraction patterns of neat films. Solution-casted neat films from PBDB-T, PBDB-S:PNDIBS and PBDBS-T on plain glass substrate. All neat films were thermally annealed at 175°C.

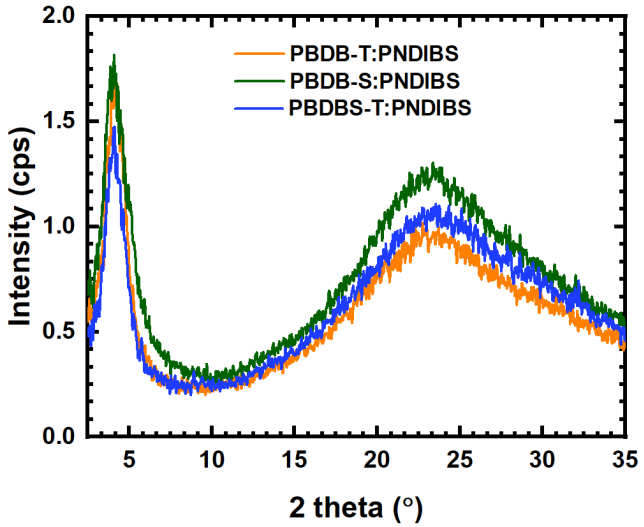

Figure S15. X-Ray Diffraction patterns of blend films. Solution-casted blend films from PBDB-T:PNDIBS (1:0.4 wt/wt), PBDB-S:PNDIBS (1:0.4 wt/wt) and PBDBS-T:PNDIBS (1:0.6 wt/wt) on plain glass substrate. PBDB-T:PNDIBS and PBDB-S:PNDIBS blend films were annealed at 175°C, while PBDBS-T:PNDIBS blend film was aged for 3hrs in a glovebox.

Table S13. X-Ray Diffraction data and mean crystallite domain sizes L_c of PNDIBS, donor polymers and their respective blends.

Blend system:	2 theta (100) (°)	d_{100} (Å)	FWHM (°)	L_c (nm)	2 theta (010) (°)	d_{010} (Å)
PBDB-T	4.44	19.85	1.45	6.07	23.42	3.79
PBDB-S	4.4	20.03	1.77	4.97	23.42	3.79
PBDBS-T	4.36	20.21	1.32	6.67	22.71	3.91
PBDB-T:PNDIBS	4.12	21.42	1.29	6.82	23.50	3.78
PBDB-S:PNDIBS	4.12	21.42	1.50	5.87	23.54	3.77
PBDBS-T:PNDIBS	4.08	21.63	1.12	7.86	23.35	3.80